5-2001

Micro-Probe for Physical and Chemical Surface Analysis

Joshua Mathews

MICRO-PROBE FOR PHYSICAL AND CHEMICAL SURFACE ANALYSIS

By

Joshua Benjamin Mathews

B.S. University of Maine, 1998

A THESIS

Submitted in Partial Fulfillment of the

Requirements for the Degree of

Master of Science

(in Chemical Engineering)

The Graduate School

The University of Maine

May 2001

Advisory Committee:

Douglas W. Bousfield, Professor of Chemical Engineering, Advisor

Adriaan Van Heiningen, Ober Chair and Professor of Chemical Engineering

Yang Xiang, Research Engineer in Chemical Engineering

MICRO-PROBE FOR PHYSICAL AND CHEMICAL SURFACE ANALYSIS

By Joshua Benjamin Mathews

Thesis Advisor: Dr. Douglas W. Bousfield

An Abstract of the Thesis Presented
in Partial Fulfillment of the Requirements for the
Degree of Master of Science
(in Chemical Engineering)
May, 2001

Non-uniform porosity of paper and coated paper is important in printing and paper making industries. Current porosity measurements give results averaged over a large area. A new method is developed to determine local variations in porosity and surface chemistry.

A measured volume of a probe liquid is applied to a hemispherical glass probe. The substrate of interest is brought into contact with the fluid drop. The resulting liquid bridge exerts a force on the probe due to surface tension forces. A video camera is used to visually correlate the physical phenomena with the force-time data.

The force-time data is recorded for substrates in four main groups: 1) non-porous, 2) model porous, 3) swellable substrates, and 4) real substrates. The force is found to be a function of the minimum fluid column radius and the surface tension of the fluid for non-

porous substrates. For porous samples, the force rapidly increases to a value and is followed by a decrease. For porous samples, this decrease is related to the radial spreading of the fluid into the porous substrate and is related to the local rate of fluid uptake. A theoretical model is proposed that describes the results on porous substrates. The model describes the shape of the force-time curves as well as the slope for a range of substrate and probe fluids. For swellable samples, the force slowly increases to a maximum and then decreases. This behavior is linked to the spreading of the fluid on the surface and the wetting delay. Real paper surface are some combination of the two behaviors.

Acknowledgements

First, I would like to thank my Lord and Savior Jesus Christ for providing the opportunity to further my education in Chemical Engineering, and for giving me the patience and perseverance to see this work through to completion.

I would like to thank my advisors Doctor Doug Bousfield, and Doctor Adriaan van Heiningen for the time that they have contributed to my research. I thank Dr. Bousfield for giving me a project that took advantage of my natural abilities. I would also like to thank Dr. van Heiningen for his insight into the theoretical aspects of my work. This project has greatly contributed to my knowledge in the area of surface science.

Thanks to my other committee member Doctor Yang Xiang for accepting to spend some time and energy during Thanksgiving break for the benefit of my thesis.

I would also like to thank all of the graduate students as well as the staff of the Chemical Engineering department for being so helpful. I dedicate a special thank you to Saybil and Dave for letting me constantly borrow their textbooks. I wish them all good luck in their future work.

Table of contents

List of Tables

List of Figures

Nomenclature

a	Surface area
a_v	Particle surface area per unit volume of particle
c_0	Contact angle parameter
d_p	Particle diameter
D_M	Diameter of the saturation front
D_p	Particle diameter
D_S	Diameter of footprint on the substrate
f	Friction factor
F	Force
F_{max}	Maximum force
F_t	Force at time t
F^{**}	Normalized force
h	Height of probe
h_p	Height of porous layer
L	Length of packed column
N_c	Number of capillaries
P_L	Pressure in packed column at length L
P_0	Pressure in packed column at the top of column
r_{min}	Minimum radius
r_p	Equivalent pore radius
r_{rough}	Roughness ratio

R	Radius
R_c	Radius of capillary
R_d	Radius of fluid drop
R_h	Hydraulic radius
$R_{profile}$	Radius of fluid bridge profile
t	Time
t_{max}	Time at maximum force
t_p	Penetration time
u	Average velocity
v_0	Superficial velocity (Blake-Kozeny equation)
v	Volume
V_d	Initial drop volume
Z	Z Cartesian coordinate direction

Greek symbols

Δp	Pressure drop
ε	Void fraction
η	Viscosity of fluid
θ	Contact angle
θ_{ap}	Apparent contact angle
θ_d	Dynamic contact angle
θ_{in}	Intrinsic contact angle
θ_L	Contact angle in liquid phase

θ_{ps}	Contact angle on probe surface
θ_{ss}	Contact angle on substrate surface
θ_S	Contact angle in solid phase
θ_V	Contact angle in vapor phase
μ	Fluid viscosity
ρ	Liquid Density
σ	Surface tension
Ω_1	Surface area of patch number 1 (Cassie equation)
Ω_2	Surface area of patch number 2 (Cassie equation)

Introduction

The porosity of a material is important for many common materials such as textiles, leather, filters, and tissue products. In the chemical process industry, the porosity of various materials such as catalysts, membranes, and packed beds, plays an important role in the process operation. The performance of various products depends on the porosity of that product. While there are standard methods to measure the large-scale porosity of materials, there is no common method to measure the local porosity of substrates on a small length scale.

Proposed test method

In order to measure the local variation in porosity of a substrate we would like to characterize a very small area on the sample. The new method to evaluate local porosity is developed by analyzing the force-time response of a small drop of fluid on a probe as it contacts a substrate. Analysis of the force-time data through a mathematical model representing the substrate will give understanding as to the chemical and physical characteristics of the substrate. This test method has the potential of determining the local porosity and porosity variation of the substrate. The ultimate goal is to use this test method to characterize the uniformity of a paper sample and possibly predict the occurrence of back trap mottle problems.

The objective of the proposed technique is able to characterize surfaces in a unique way. It should quantify the short time fluid uptake or spreading of fluid in a small spot on the substrate. Since the uptake is related to the porosity of the surface layer and the local surface chemistry it is anticipated that the present technique will be able to characterize the variation of porosity or surface chemistry in area wetted by the test liquid.

Chapter 1: Literature Review

While there are standard methods to measure the large-scale porosity of materials, there is no common method to measure the local porosity of substrates on a small length scale. Recently, Xiang *et. al*, (1999) link porosity variations or pore structure variations in a paper coating layer to a printing defect called "back-trap mottle". A small-scale (~1 mm) variation in substrate properties leads to a variation in ink density. Xiang *et. al*, (2000) showed that small regions of closed and open areas may cause ink setting rate differences.

1.1 Back-trap Mottle

The printing problem called "back-trap mottle" occurs only with multiple printing units. In multi –color offset printing, part of the free ink on the paper transferred from the previous printing unit may transfer or "backtrap" ink to the non-image areas of subsequent blankets. If ink sets in a non-uniform manner from one impression to another, the local ink transfer balance will be disrupted and a mottled image may result. Back-trap mottle is a defect involving the non-uniform setting on coated paper and may have several different causes. For the most part, it is thought to result from the local variation in coating absorbency. Recently much investigation has been done by several authors in order to link back-trap mottle to a specific cause (Isoard, 1983; Aschan, 1986; Lyne, 1986; Nelson, 1986; Nishioka, *et al*, 1986; Arai, *et al*, 1988; Engstrom, *et al*, 1987; Aspler and Lepoutre, 1991; Whalen-Shaw and Eby, 1991; Louman, 1991; Kumana, *et al*,

1993; Gane, *et al*, 1994; Plowman-Sandreuter, 1994; Engstrom, 1994; Miwata, H., *et al*, 1995). Many believe back-trap mottle is caused by uneven distribution of binder at the coating surface while others believe the non-uniformities in surface roughness is a major factor and still others believe that the mass distribution of the coating layer plays an important role. Whether it is the lack of surface smoothness uniformity, pore structure, or chemical composition; they are all surface phenomena in the top 1-2 μm of the coating layer.

This printing defect cannot be detected by standard laboratory techniques at present. The defect can only be seen after printing. There is a large cost to paper makers when a shipment of paper is returned because of this printing defect. Therefore it is important to find a laboratory method to detect this problem right after production. Also it could then be used as a tool to find alternative production conditions and methods to minimize or eliminate this small-scale porosity variation, which is responsible for back-trap mottle.

1.2 Spreading on non-porous substrates

The spreading of fluid on non-porous surfaces has been a subject of numerous theoretical and experimental studies. Viscous and surface tension forces govern the dynamics of a drop spreading on non-porous surfaces. As a drop of fluid contacts a surface, it will orient itself to form a shape of least surface energy. The surface tension forces of the fluid and the surface energy of the substrate dictate the resulting shape of the drop.

We consider a drop of liquid resting on an ideal solid surface and in equilibrium with its vapor, as shown in Figure 1.1. An ideal solid surface is a perfectly smooth, non-porous, chemically homogeneous, rigid, insoluble and non-reactive surface.

The angle between the drop and the surface, measured within the liquid, is called intrinsic contact angle θ_{iv} and is given by the Young equation (Israelachvili 1992):

$$\cos(\theta_{in}) = \frac{\sigma_{SV} - \sigma_{SL}}{\sigma_{LV}} \tag{1.1}$$

where σ is the interfacial tension between two phases, and S, L, and V stand for solid, liquid, and vapor, respectively. The contact angle calculated from the Young equation represents the state of minimum energy of the drop on the surface.

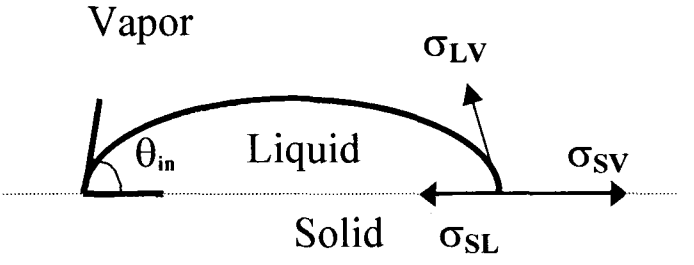

Figure 1.1: Intrinsic contact angle

In the case of rough substrates, the intrinsic contact angle θ_{in} given by the Young equation may be different than the apparent contact angle θ_{ap} given by optical measurements. For smooth surfaces, those two angles are equal. However, they can be very different on rough substrates, as shown in Figure 1.2. The contact angle measured

in static conditions is the apparent contact angle. It is often referred as the static contact angle θ.

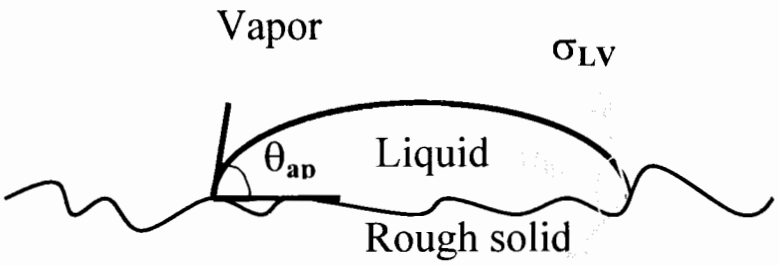

Figure 1.2: Apparent contact angle

Wenzel (1936) developed an equation giving the apparent contact angle θ_{ap} as a function of the intrinsic contact angle θ_{in} in the case of a rough surface.

$$\cos(\theta_{ap}) = r_{rough}\cos(\theta_{in}) \tag{1.2}$$

The roughness ratio r_{rough} is the ratio of the true surface area of the rough solid to its nominal surface area. If θ_{in} is smaller than 90 degrees, θ_{ap} decreases as the roughness increases. On the contrary, if θ_{in} is larger than 90 degrees, θ_{ap} increase as the roughness increases.

Most of the real surfaces present chemical or chemical surface heterogeneities. Cassie (1948) developed an equation giving the apparent contact angle for heterogeneous surfaces. It states that the cosine of the apparent contact angle on a heterogeneous surface is the weighted average of the cosines of the contact angles on the various patches of the surface. If Ω_1 and Ω_2 represent the surface areas of two patches with respective

contact angles θ_1 and θ_2, then the contact angle θ_{ap} of the heterogeneous surface is given by:

$$\cos(\theta_{ap}) = \Omega_1 \cos(\theta_1) + \Omega_2 \cos(\theta_2) \tag{1.3}$$

1.3 Spreading on a porous substrate

Spreading on a porous substrate is important to understanding the physical makeup of a substrate. There are two successive phenomena that influence drop spreading. The first is mechanical spreading due to dissipation of inertial forces. The second and more important one is capillary forces due to the penetration of the liquid into the pores of the substrate (Oliver, 1984).

Measuring contact angles on porous substrates present a difficulty due to absorption and the heterogeneity of the surface. A single steady value does not exist because the drop shape is changing. Elftonson and Strom (1995) measured the contact angles of aqueous solutions on model porous and non-porous substrates. They found that the initial contact angle on the porous material is higher than on the non-porous material when the angle is high. This is expected due to the composite character (containing air and solid) of the porous materials. For lower contact angles, the initial contact angle is lower on the porous material than on the non-porous material. This is mostly due to the high penetration of the liquid into the pores and a lateral spreading induced by surface capillaries. Initial penetration and capillary-induced spreading are promoted by low equilibrium contact angles.

1.4 Absorption into a porous substrate

Knowledge of capillary action is necessary in order to understand absorption into a porous substrate. The liquid permeability depends on the liquid viscosity, surface tension, porous structure, penetration depth, time and liquid polarity. In the case of paper or coatings, the anisotropic structure, the tortuosity and the swelling of the fibers in the presence of a polar liquid influence the liquid permeability as well (LePoutre, 1977). Capillarity plays an especially important role in the dynamics of printing. The quality of the printed image depends on the wicking of the ink into the substrate.

A porous substrate can be modeled as a bundle of tiny capillaries, each of radius R. Adamson (1990) shows that the driving force for wicking is the capillary pressure difference Δp, which, is given by the Young-Laplace equation as:

$$\Delta p = \frac{2 \cdot \sigma}{R} \cos(\theta_d) \tag{1.4}$$

where σ is the surface tension of the liquid and θ_d is the dynamic contact angle of the fluid inside the capillary. Based on this single capillary model, Middleman (1995) develops a simple dynamic model of a drop, initially sitting on a porous surface, wicking into a porous media below the surface. In the development of this simple model, the wetted diameter of the drop or the contact area of the drop is assumed to be independent of time, within radius R_d. The interface between the drop and the paper is considered the end of a bundle of capillaries, all with individual radii of R_c. The void fraction ε of the surface is given by:

$$\varepsilon = \frac{N_c \cdot \pi \cdot R_c^2}{\pi \cdot R_d^2} \tag{1.5}$$

where N_c is the number of capillaries that open into the footprint of the drop. The average velocity u of the flow into a single capillary follows from the Lucas-Washburn equation:

$$u = \frac{dx}{dt} = \left(\frac{\sigma \cdot R_c \cdot \cos(\theta_d)}{8 \cdot \eta \cdot t} \right)^{\frac{1}{2}}. \tag{1.6}$$

If V is the volume of the drop on the surface, the volume flow rate is:

$$\frac{-dV}{dt} = \pi \cdot u \cdot \varepsilon \cdot R_d^2. \tag{1.7}$$

Assuming that the radius of the drop on the surface is constant, the volume of the liquid remaining at the surface is given by:

$$V(t) = V_d - \pi \cdot \varepsilon \cdot R_d^2 \left(\frac{\sigma \cdot R_c \cdot \cos(\theta_d)}{2 \cdot \eta} \cdot t \right)^{\frac{1}{2}} \tag{1.8}$$

where V_d is the initial volume of liquid.

The penetration time t_p is obtained by stating that V=0 at t_p.

$$t_p = \frac{2 \cdot \eta}{R_c \cdot \sigma} \cdot \left(\frac{V_d}{\pi \cdot R_d^2 \cdot \varepsilon \cdot (\cos(\theta_d))^{\frac{1}{2}}} \right)^2 \tag{1.9}$$

One of the main theoretical approaches to flow through a packed bed is considered by regarding a column full of a bundle of tangled tubes of weird cross section as discussed by Bird *et al* (1960). The packing material may be spheres, cylinders, or various kinds of shapes. It is assumed that the packing is uniform everywhere, the packing is small in comparison to the column diameter, and the column diameter is constant.

He defines the friction factor for the packed bed as:

$$\frac{P_0 - P_L}{\frac{1}{2} \cdot \rho \cdot v_0^2} = \frac{L}{D_p} \cdot 4f \tag{1.10}$$

in which D_p is the particle diameter and v_0 is the "superficial velocity" (this is the average linear velocity the fluid would have in the column if no packing were present); L is the length of the packed column. For laminar flow in circular tubes of radius R it is seen that:

$$\langle v \rangle = \frac{(P_0 - P_L) \cdot R^2}{8 \cdot \mu \cdot L} \tag{1.11}$$

Now if we imagine the packed bed as a tube of very complicated cross section with a hydraulic radius R_h, the average flow velocity in the cross section available for flow is then:

$$\langle v \rangle = \frac{(P_0 - P_L) \cdot R_h^2}{2 \cdot \mu \cdot L} \tag{1.12}$$

The hydraulic radius may be expressed in terms of the "void fraction" ε and the wetted surface area *a* per unit volume as:

$$R_h = \frac{\varepsilon}{a} \tag{1.13}$$

The quantity *a* is related to the "specific surface" a_v (the total particle surface/the volume of the particles) by:

$$a = a_v(1 - \varepsilon) \tag{1.14}$$

The quantity a_v is in turn used to define the mean particle diameter D_p:

$$D_p = \frac{6}{a_v} \tag{1.15}$$

He chooses this definition because, for spheres, Eq. 1.15 gives just D_p=diameter of sphere. Then if we combine these definitions with Eq. 1.12, we obtain:

$$v_0 = \frac{(P_0 - P_L)}{L} \cdot \frac{D_p^{\,2}}{2 \cdot (36 \cdot \mu)} \cdot \frac{\varepsilon^3}{(1-\varepsilon)^2} \tag{1.16}$$

Experimental measurements indicate that the theoretical formula can be improved if the 2 in the denominator on the right-hand side is changed to a value somewhere around 4 or 5. The analysis of a great deal of data has led to the value 25/6, which is accepted here. By inserting that value it gives:

$$v_0 = \frac{(P_0 - P_L)}{L} \cdot \frac{D_p^{\,2}}{150 \cdot \mu} \cdot \frac{\varepsilon^3}{(1-\varepsilon)^2} \tag{1.17}$$

which is the Blake-Kozeny equation. This result is generally good for void fractions less then 0.5 and is valid only for the laminar region of flow.

1.5 Current porosity testing techniques

Porosity is important to a number of substances and products. Porosity testing is an important part of paper surface characterization. Several pore characterization techniques have been developed.

Fluid absorption is a common method to measure porosity or void fraction. A silicon oil absorption method developed by LePoutre and Rezanowich (1977) is used to determine the total void volume and void fraction of a porous sample. Void fraction is determined by measuring the difference in mass of a sample before and after being saturated with

silicon oil. The mass and volume of silicon oil absorbed is calculated. Although void fraction and total void volume are calculated, this test gives an average void fraction over the entire surface of a sample.

Bristow (1967) designed an instrument to study dynamic penetration and wetting of paper. A paper strip is mounted to a rotating wheel and is drawn past a miniature headbox, which rests on the paper strip. The headbox is filled with a known amount of fluid which has enough time for absorption determined by the speed of the wheel and width of the slice opening. Since the speed can be varied, a relationship between the amount of liquid transferred and the time for absorption can be established. This method analyzes the bulk permeability of a sample rather than local permeability.

Forced air permeability measurement can also be done to characterize the pore structure of a sample. TAPPI test methods (1991) report a standard method where the flow through a sample is determined by collecting a gas that passes through the pores of the sample into a sealed container. Flow is then calculated from the rate of pressure increase in the sealed container over time. This technique determines sample permeability of the bulk but not on a local level. This can be related to porosity with certain assumptions.

Capillary flow porometry described by Mark (1984) is another method for pore analysis. A fully wetted sample is placed in the sample chamber and the chamber is sealed. Gas is then allowed to flow through the chamber behind the sample. When the pressure reaches a point that can overcome the capillary action of the fluid within the pore (largest pore),

the bubble point has been found. After determination of the bubble point, the pressure is increased and the flow is measured until all pores are empty, and the sample is considered dry. This method is able to determine pore size distribution, mean pore size, and liquid permeability. A disadvantage is that porometry determines "through" pore diameter, distribution, and permeability. Porometers measure flow through the material, and therefore characterize only "through" pores. Porometers thus yield no useful information about "dead-end" pores, but are useful for determining flow through the sample material.

Another well-known method of porosity analysis is mercury porosimetry. This technique first proposed by Washburn (1921), uses mercury intrusion to determine pore volume. A sample is placed into a sample chamber then mercury is introduced. A vacuum is created in the chamber and a volume is recorded. The sample is not initially intruded with mercury because of its high surface tension. Gradually increasing amounts of pressure are applied. For each incremental increase in pressure, the change in intrusion volume is equal to the volume of the pores whose diameters fall within an interval that corresponds to the particular pressure interval. This method is able to give measurements of mean pore size, pore size distribution, bulk density, total pore volume, and particle size distribution. However, this technique gives no information as to fluid absorption rates into the pores of a sample under ambient conditions. This method requires relatively large samples compared to the length of interest.

Chapter 2: Description and Validation of Test Method

2.1 Test equipment

A new method to evaluate local porosity is developed by analyzing the force-time response of a small drop of fluid on a probe as it contacts a substrate. A schematic of the test method is shown in Figure 2.1. A small drop of fluid is applied to the tip of the probe. The substrate is raised to the probe until a fluid bridge is formed between the probe and the substrate. The force that the fluid exerts on the probe due to the surface tension of the fluid bridge is measured by a microbalance that the probe is suspended from. The device used to gather data is a microbalance (Sigma70 manufactured by KSV). The device is computer controlled and user programmable. Its normal use is to measure surface tension of dynamic contact angles, the absorption behavior of solids, surface recovery and dehydration rate measurements. The balance is equipped with two hooks, which makes it possible to apply a counter weight. The accuracy of the balance was checked. A small piece of wire was weighed and attached to the probe. The balance recorded a weight of 309 μN. The same piece of wire was weighed on a different balance and was found to have a weight of 307 μN.

Some preliminary tests were conducted using a flat tipped cylindrical probe. The particular geometry of the flat probe demands that the horizontal surface to which the fluid is applied, be perfectly parallel to the substrate surface. The correct experimental

conditions were difficult to achieve and thus the probe was abandoned. A probe with a hemispherical probe tip was then used because minor misalignment is now no longer an issue. A hemispherical probe also allows with relative ease to measure the contact angle, while the contact angle is not easily measured from a sharp 90-degree edge of a flat cylindrical probe tip. A glass probe and several plastic probes were considered. The glass probe was selected to be the standard probe because it is chemically inert and its surface properties are well known. The hemispherical probe was constructed from a glass capillary tube with an outside diameter of 6.5 millimeters. Then the tube was heated until the glass began to melt, upon subsequent cooling a probe with a hemispherical tip was obtained.

Care must be taken when applying the fluid drop to the probe. The drop is placed as near to the center of the probe as possible using a syringe.

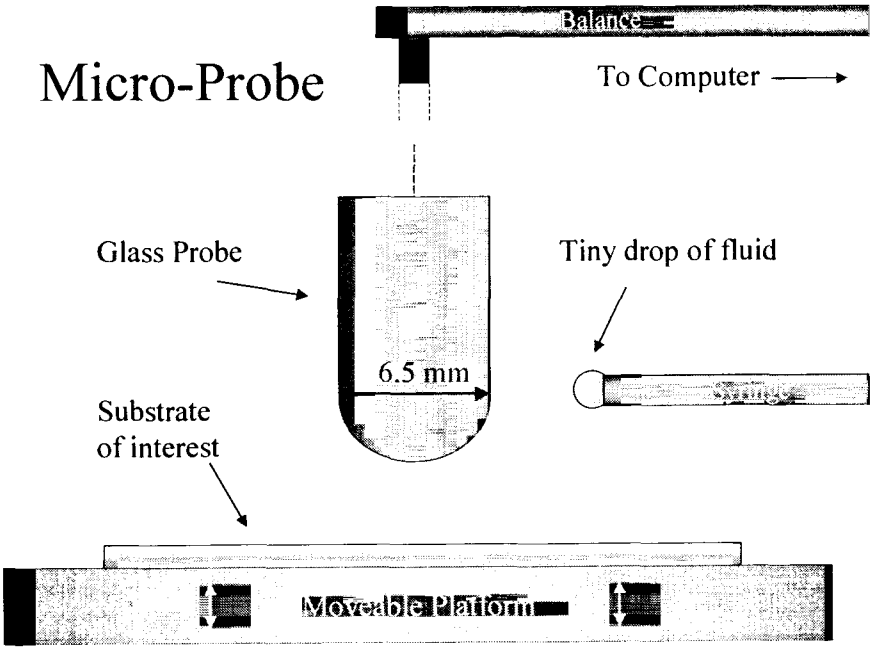

Figure 2.1. Micro-probe setup

The substrate is then raised until the fluid on the probe comes into contact with the substrate. When the drop of fluid contacts the substrate, a liquid bridge is formed between the probe and the substrate as depicted in Figure 2.2. The shape of the liquid bridge is determined by minimization of its surface energy.

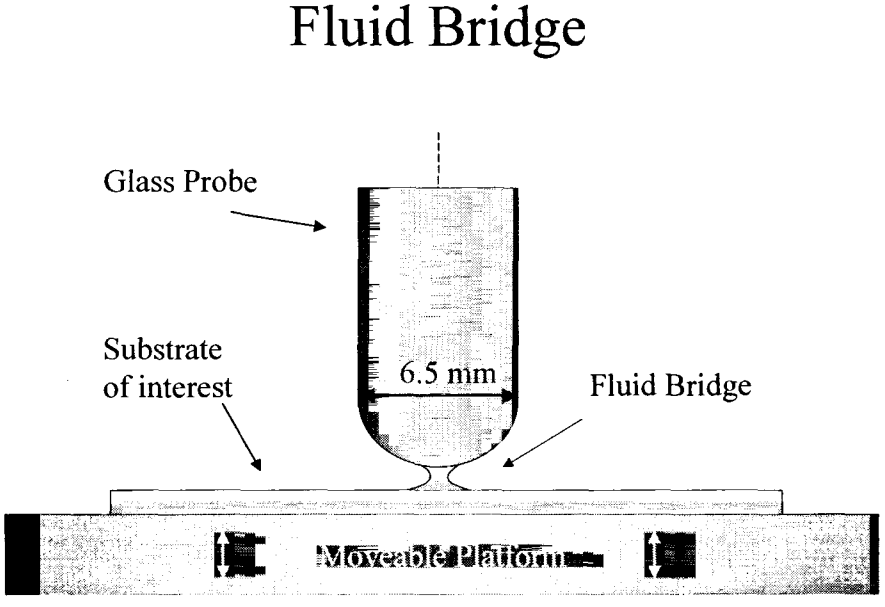

Figure 2.2. Liquid bridge formed.

2.2 Force calculation

The force is recorded as a function of time and stored on a computer. When water is used as a fluid, after the initial contact, the force quickly reaches a maximum and then decreases until the filament of fluid breaks due to evaporation of the water. To validate the concept and to check the equipment, a series of tests on non-porous substrates were done. Glass, Mylar™, and Teflon™ were used as substrates with quite different surface energies. The three model fluids used were water, silicon oil, and ethylene glycol. Table 2.1 shows the drop contact angles for all the fluid and substrate combinations. The fluids

were selected because of their diverse physical characteristics. Also, ethylene glycol and silicon oil do not evaporate, and thus a constant force is obtained on these non-porous substrates.

	Water	Silicon Oil	Ethylene Glycol
Glass	48	15	40
Mylar	62	18	35
Teflon	98	28	85

Table 2.1: Drop contact angle in degrees for fluid and non-porous substrates

When considering the geometry of the fluid column as in Figure 2.3, an internal pressure in the fluid is generated by the curvature of the meniscus of the fluid bridge. The force of the fluid on the probe can be described by a closed form expression within 10% of those obtained by exact solution of the Young-Laplace equation as (Pitois et al. 2000):

$$F = \pi \cdot r_{\min} \cdot \sigma \cdot \left(1 + \frac{r_{\min}}{R_{profile}}\right) \tag{2.1}$$

where r_{min} is the minimum radius of the fluid column, σ is surface tension, and $R_{profile}$ is the radius of the meridian profile.

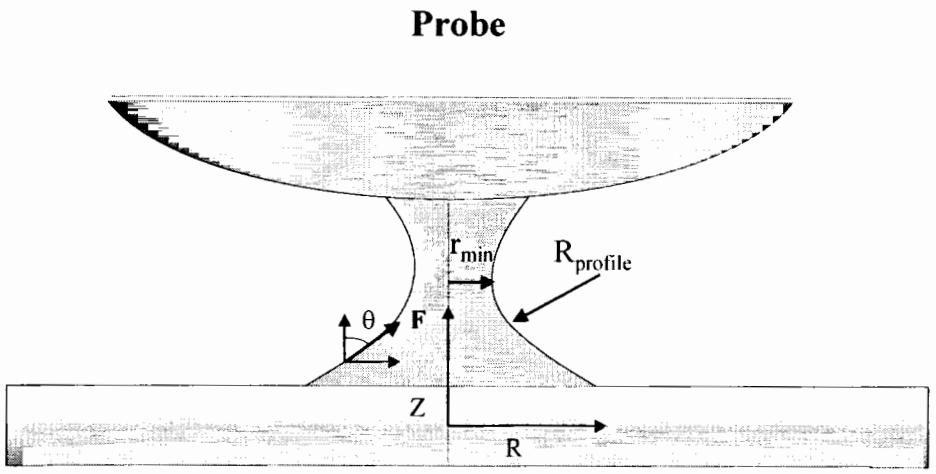

Figure 2.3: Fluid bridge radii of curvature.

A simpler expression of the force exerted by the liquid bridge can be obtained by neglecting any pressure effects and considering the surface tension forces at the minimum radius of the bridge which are parallel to the axis of the liquid column. The expression for the force becomes:

$$F = 2 \cdot \pi \cdot r_{min} \cdot \sigma \tag{2.2}$$

The minimum radius of the fluid bridge, r_{min}, and the radius of the meridian profile, $R_{profile}$ can be measured using a video camera and image analysis through the ImagePro software program. In order to test the accuracy of Eqs. (2.1) and (2.2) the video analysis was done for the system of water on a glass substrate for probe heights of 0.25, 0.35, and 0.45 mm. As the water evaporates, the radii of curvature changed. An image was analyzed every 20 seconds after the start of each experiment to determine r_{min} and $R_{profile}$

at that instant. The force was calculated considering pressure effects (Eq. 2.1) and without considering pressure effects (Eq. 2.2). These two force profiles were plotted together with the experimental results in Figures 2.4 to 2.6.

The force calculated using Eq. (2.1) is noisier because of inaccuracies in determining the radius of curvature of the meridian profile. The calculated values for Eq. (2.1) do not match well with experimental data but do show some of the correct trends. Eq. (2.2) shows a result within 20%. Similarly, in their attempt to measure the force between a sphere and a flat plate, Mason & Clark (1965) found difficulty matching the calculated and experimental forces. For the case of a 0.25 mm gap in Fig. 2.4, Eq. (2.1) over predicts the force. However, the predicted shape is correct. The initial increase in the force is calculated because the ratio of r_{min} to $R_{profile}$ increases faster than r_{min} is decreasing. For the other two cases, the initial rounding is not significant. However, it is clear from Figures 2.4-2.6 that Eq. 2.2 generally gives a better prediction of the absolute value of the measured force, although at the larger gap of 0.45 mm the two formula's have essentially the same predicting power. Presently it is not clear why Eq. (2.1) over predicts the measured results.

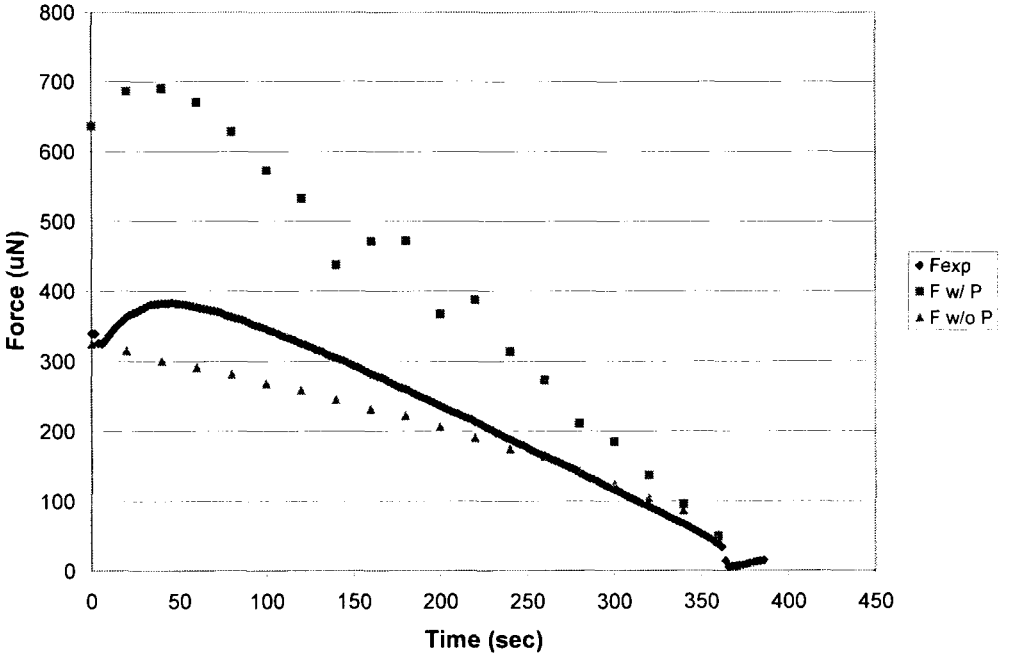

Figure 2.4: Plot of experimental force, force calculated with pressure forces, force calculated without pressure forces considered for a gap of 0.25 mm.

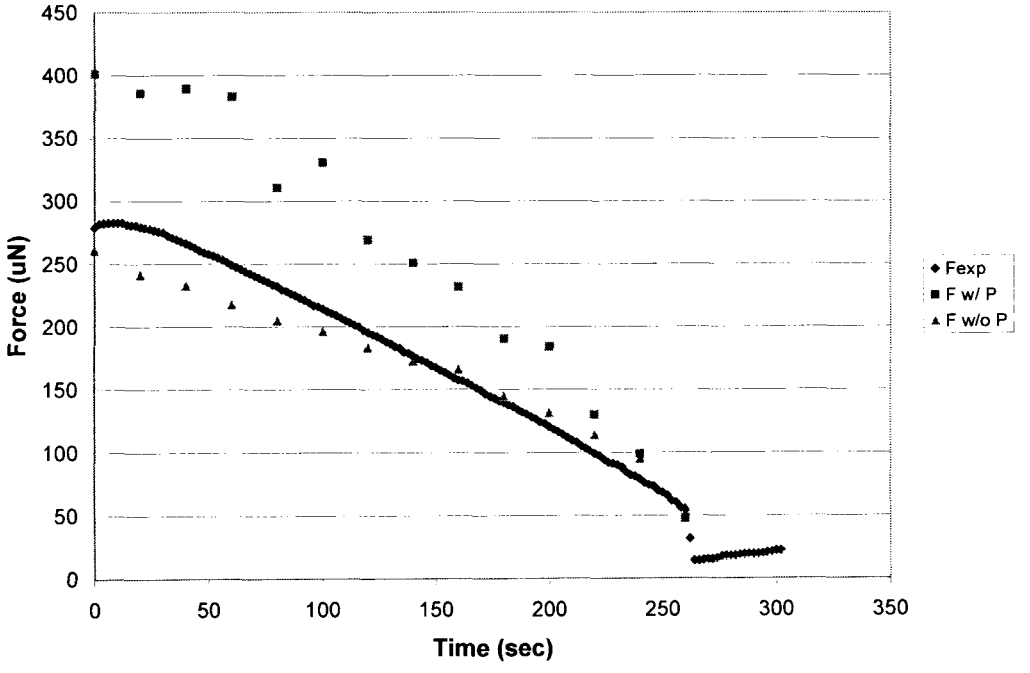

Figure 2.5: Plot of experimental force, force calculated with pressure forces, force calculated without pressure forces considered for a gap of 0.35 mm.

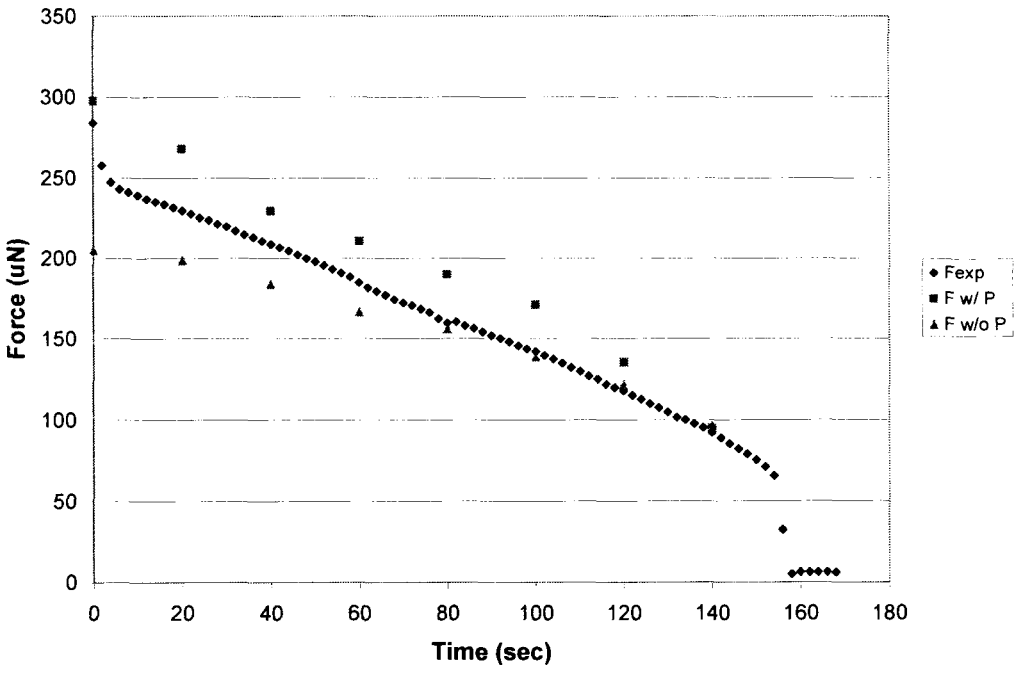

Figure 2.6: Plot of experimental force, force calculated with pressure forces, force calculated without pressure forces considered for a gap of 0.45 mm.

Since it was found that the force calculated using Eq. 2.2 gave a relatively good approximation of the measured force over the range of the experiments for different heights, all the subsequent force calculations will be based on this formula. Further evidence of the validity of Eq. (2.2) is seen in Figures 2.7 to 2.9 in which the experimental and calculated force are compared.

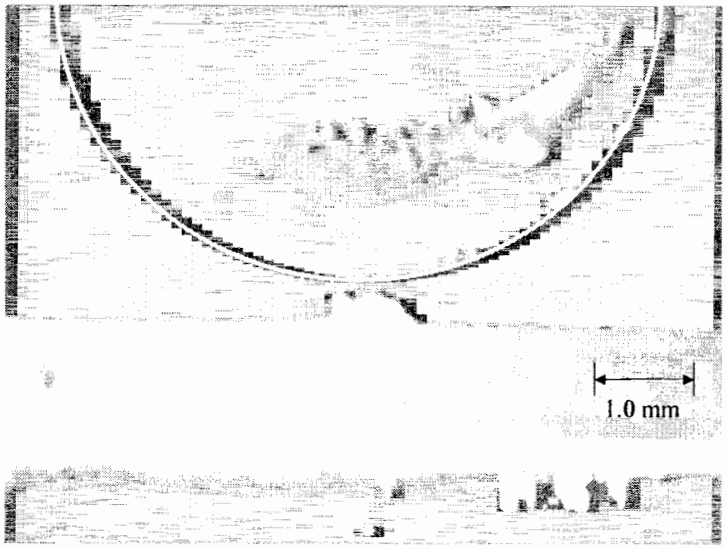

V=0.5μL H=0.33 mm

Calculated Force = 294μN
Experimental Force ~ 305μN

Figure 2.7: Experimental and calculated force with Eq. (2.2) for water on glass.

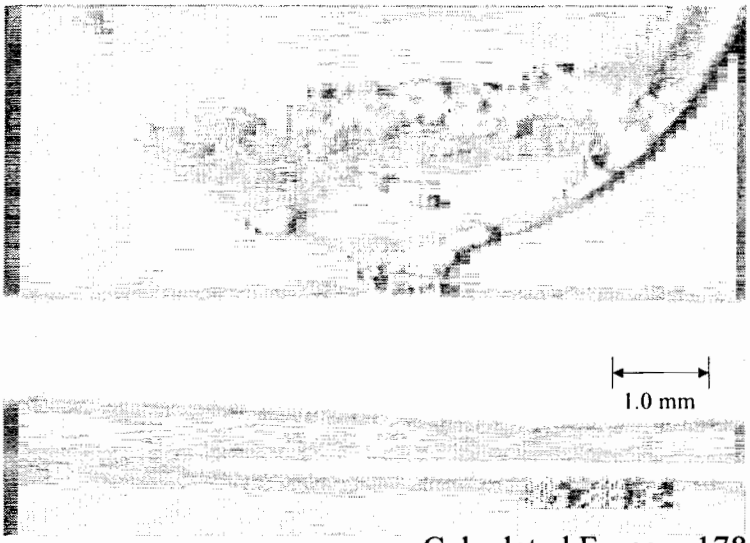

V = 0.5μL H = 0.33 mm

Calculated Force = 178μN
Experimental Force ~165μN

Figure 2.8: Experimental and calculated force with Eq. (2.2) for water on Teflon™.

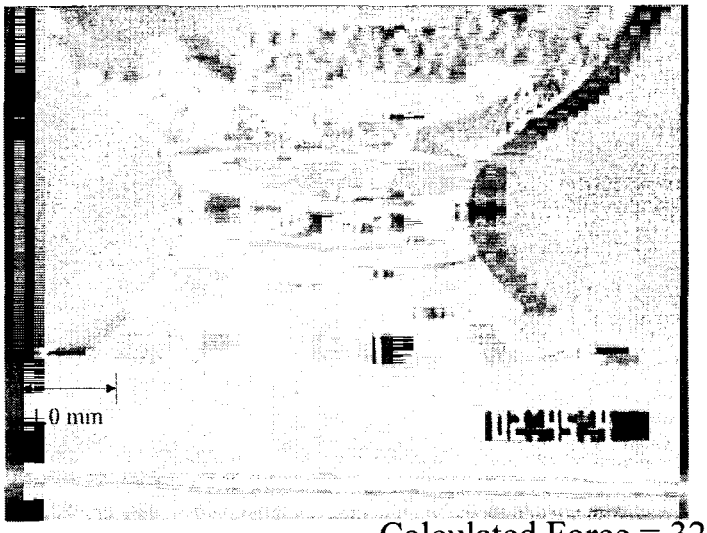

V = 24.6μL H = 1.57 mm Calculated Force = 328μN

Experimental Force ~ 315μN

Figure 2.9: Experimental and calculated force with Eq. (2.2) for silicon oil on glass.

Tables 2.2-2.4 list the results for different heights of the probe from the substrate and all combinations of fluids and substrates. The difference between the calculated and experimental force is generally less than 20%. A sample error analysis accounting for the inaccuracy in measurement of the parameters used to calculate the force for non-porous substrates are seen in Appendix A.

	height (mm)	Minimum Diameter (mm)	Exp. Force (μN)	Calculated Force (μN)	Percent Error
Glass	0.25	1.19	305	272	11%
	0.35	0.97	192	222	-16%
	0.45	0.77	140	176	-26%
Mylar	0.25	1.19	260	272	-5%
	0.35	0.95	198	218	-10%
	0.45	0.77	138	176	-27%
Teflon	0.25	1.01	196	230	-17%
	0.35	0.77	150	176	-17%
	0.45	0.55	105	126	-20%

Table 2.2: Experimental and calculated forces found using 0.5 μL of water.

	height (mm)	Minimum Diameter (mm)	Exp. Force (μN)	Calculated Force (μN)	Percent Error
Glass	0.25	1.04	251	239	5%
	0.35	0.93	202	213	-6%
	0.45	0.82	171	188	-10%
Mylar	0.25	1.08	258	247	4%
	0.35	0.97	212	222	-5%
	0.45	0.84	179	193	-8%
Teflon	0.25	1.04	277	239	14%
	0.35	0.93	229	213	7%
	0.45	0.81	197	184	7%

Table 2.3: Experimental and calculated forces found using 0.5 μL of silicon oil.

	height (mm)	Minimum Diameter (mm)	Exp. Force (μN)	Calculated Force (μN)	Percent Error
Glass	0.25	1.28	301	293	3%
	0.35	1.12	214	255	-19%
	0.45	0.99	236	226	4%
Mylar	0.25	1.37	361	314	13%
	0.35	1.17	287	268	7%
	0.45	1.01	232	230	1%
Teflon	0.25	1.28	313	293	6%
	0.35	1.08	275	247	10%
	0.45	0.99	238	226	5%

Table 2.4: Experimental and calculated forces found using 0.5 μL of ethylene glycol.

When the probe is moved closer to the surface, the minimum radius increases and the force increases. As the probe moves away, the opposite is seen. Eq. (2.2) generally under predicts the measured force when water is used as the fluid, while an over prediction is seen for ethylene glycol.

2.3 Force vs. contact angle

The minimum radius of the fluid determines the magnitude of the force between the probe and the substrate. When considering the geometry of the fluid bridge, we conclude that when the contact angle of the fluid with the substrate is at 90°, r_{min} is at a maximum. For contact angles greater or less than 90°, r_{min} will be lower and result in a lower force. The contact angle between the fluid and the substrate is a direct result of the surface tension of the fluid and the surface energy of the substrate. This is seen in Fig. 2.10.

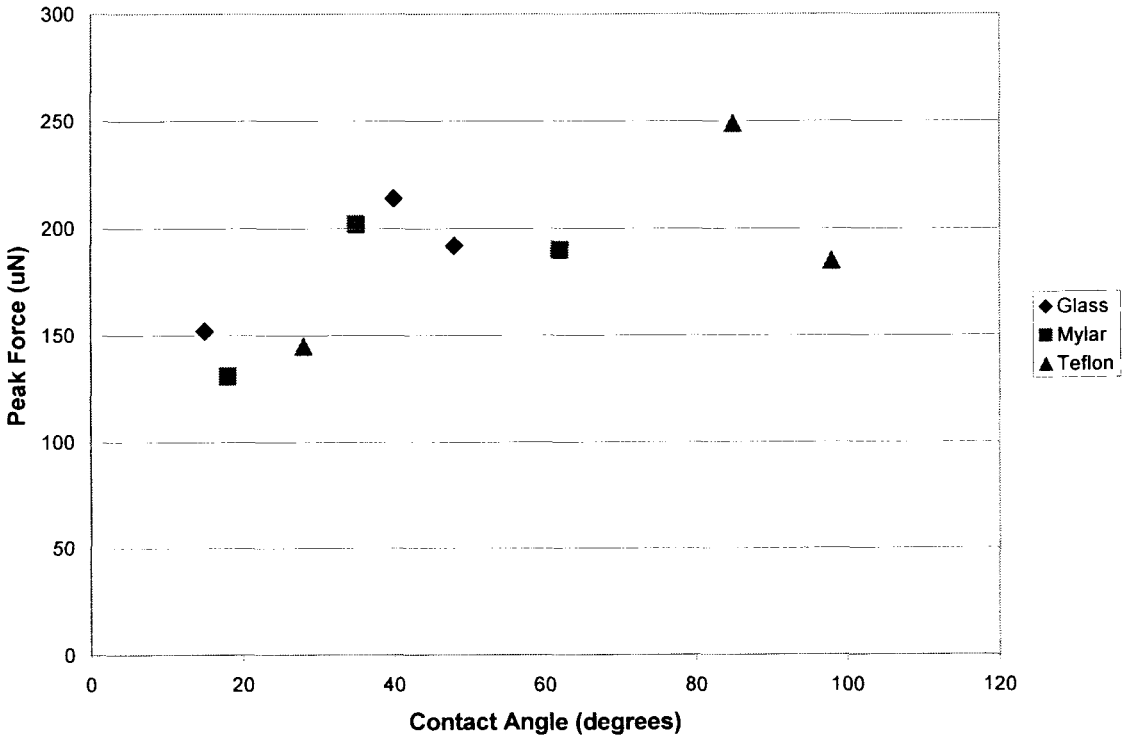

Figure 2.10: Plot of peak force vs. contact angle for water, silicon oil, and ethylene glycol on the three non-porous substrates at a gap of 0.35 mm with 0.5 μL.

In order to compare all data regardless of probe height or fluid used, the force was normalized as:

$$F^{**} = \frac{F}{\sigma \cdot \left(\frac{v}{\pi \cdot h}\right)^{\frac{1}{2}} \cdot \left(1 + \left(\frac{v}{\pi \cdot h^3}\right)^{\frac{1}{2}}\right)} \tag{2.3}$$

where F is the measured force, σ is the surface tension, v is the drop volume, and h is the height of the probe above the substrate. Figure 2.11 shows force versus contact angle after normalizing it to account for different values of surface tension, probe height, and

drop volume. An expected grouping of the data did not form. Some other factor must be causing a spread in the data.

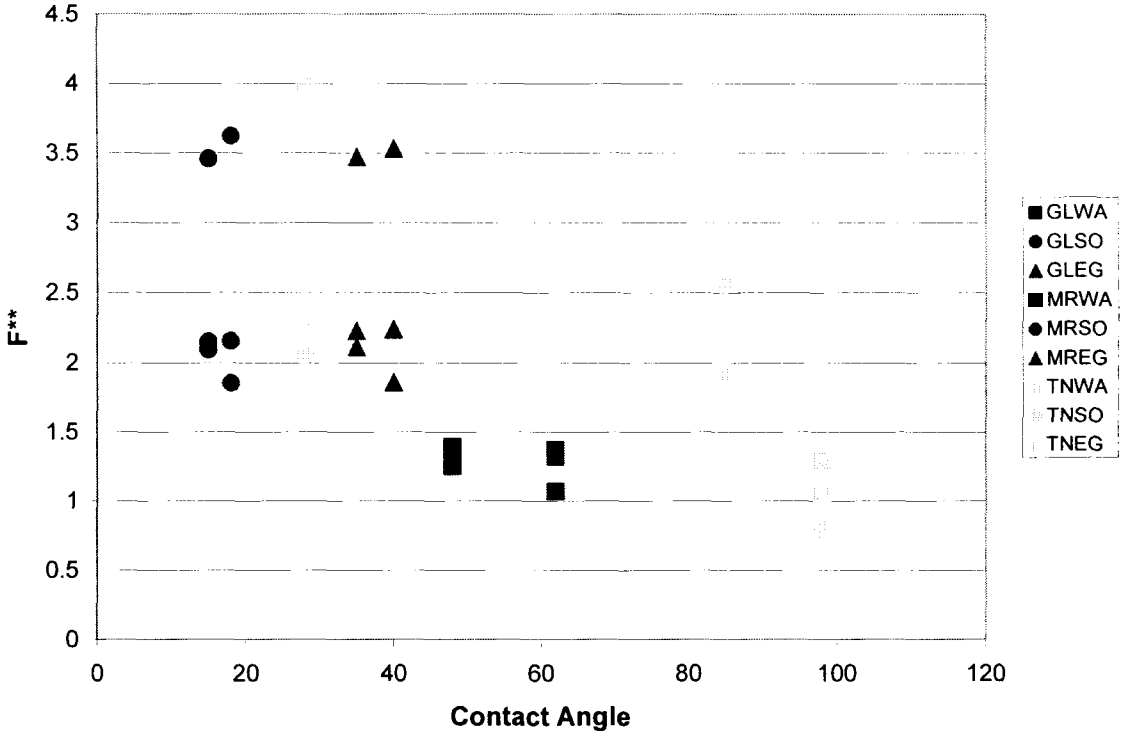

Figure 2.11: Normalized force versus contact angle for all three heights, all three fluids, and all three substrates. Dark, medium, and light symbol are for glass, Mylar™, and Teflon™ respectively. Square, circle, and triangle are for water, silicon oil, and ethylene glycol respectively.

2.4 Summary

The method to measure the force exerted by a liquid bridge is established. The force is a function of the surface tension of the fluid the distance of separation between the probe and substrate, and by the volume of the liquid applied. It can be calculated from the

measured minimum bridge radius. The bridge radius is a function of how the fluid spreads on the surface, and is a function of the contact angle and thus the magnitude of the peak force is dictated by the surface energy of the substrate.

Chapter 3: Model Porous Substrates

When the liquid bridge forms between the probe and the porous substrate, a dynamic force exerted by the liquid bridge on the probe, and thus on the microbalance is found. The change in the force can be related to the rate of absorption of fluid into the pores. The goal of this chapter is to develop this relationship and to test it using seven substrates and three fluids.

3.1 Materials

Three samples were formed by casting plastic pigments into wafers on a Teflon sheet. The three substrates are comprised of three different latex polystyrene pigments, Dow PP 722 HS, Dow PP 755 ANA, and Dow PP 788 ANA, with 0.45, 0.23, and 0.1 μm average diameters, respectively. These are chosen because the flow in the packed beds of spheres of theses samples can be described by well established equations.

Two substrates are formed by coating plastic film (Mylar™ by DuPont) with the 0.45 μm polystyrene spheres (Dow PP722 HS). The samples have 10 and 20 parts per hundred of Styrene-Butadiene latex binder (Dow 620 ANA). Latex binder is added to give strength to the coating and to decrease the void fraction.

Two other samples are porous inkjet media. Media A is a commercial product (Epson # S0 41072). Media B is a similar product but not commercial at the present time. The media are composed of a plastic base sheet with surface treated pigment particles.

The physical characteristics of each of the model porous substrates are listed in Table 3.1. The pore size distribution was determined using mercury porosimetry (Pore Sizer 9320, made by Micromeritics) however, the pure plastic pigment samples are too brittle for the test and reliable results could not be obtained. Lee *et al.* (1982) and Xiang *et al.* (2000) found that for spherical coating particles, the equivalent pore radius is approximately equal to one-third of the particle diameter. Therefore the equivalent pore radii of the 5 samples prepared from the plastic pigments are estimated as 1/3 of the diameter of the pigment particles. For the inkjet media A and B, the particle diameters are unknown but are estimated to be three times the dominant pore size as measured by mercury porosimetry. However this estimation is only an approximation because of the complex nature of these media.

The determination of the void fraction was obtained using a silicon oil absorption method. After the mass and surface area of the samples are measured, the samples are immersed in silicon oil for two days, removed from the oil, wiped clean to remove any surface oil and the wet mass is recorded. The thickness of the porous coating layer is measured using a Stylus Profilometer (Alpha-step 200, made by Tencor Instruments). Knowing the specific gravity of silicon oil, the thickness of the porous layer, the volume

of silicon oil absorbed, the surface area, and mass of the sample allows the void fraction to be estimated.

Substrates		Media A	Media B	PP10pph	PP20pph	722	755	788
Equivalent Pore Radius	μm	0.015	0.020	0.150	0.150	0.150	0.077	0.033
Particle Diameter	μm	0.045	0.060	0.450	0.450	0.450	0.230	0.100
Height of Porous Layer	μm	40	46	60	48	1000	1000	1000
Void Fraction		0.35	0.39	0.35	0.24	0.23	0.29	0.2
Contact angles @ 0.1 sec								
Water	°	33	56	37	55	19	11	19
Silicon Oil	°	17	12	14	11	11	12	15
Ethylene Glycol	°	20	26	20	30	23	24	27

Table 3.1: Physical properties of the model porous media

Another measured parameter is the diameter of the fluid column footprint. The diameter of the footprint is measured with a video camera and calculated using the ImagePro visual analysis program. Average diameters are measured for each fluid-substrate combination as seen in Table 3.2.

Diameter of Wetting (mm)	Water	Silicon Oil	Ethylene Glycol
Epson	1.28	1.04	1.37
Mercury	1.06	0.98	1.25
PP10pph	1.22	0.90	1.20
PP20pph	1.20	1.09	1.20
722	1.09	0.64	1.00
755	0.98	0.60	1.16
788	1.16	0.69	1.03

Table 3.2: Diameter of initial fluid column footprint for fluid-substrate combinations

The model fluids are water, silicon oil, and ethylene glycol. These fluids are chosen because of their different properties.

	Surface Tension mN/m	Viscosity Pa*s
Water	72.8	1
Silicon Oil	35.8	5
Ethylene Glycol	48.4	26

Table 3.3: Physical properties of model fluids

Manufacturers data are recorded in Table 3.3. Water is a polar fluid with a high surface tension and low viscosity. However because of the significant vapor pressure, water also disappears by evaporation besides being absorbed into the porous samples. The silicon oil used does not evaporate and has a viscosity five times greater than water, and a lower surface tension. Because of the low surface tension, the silicon oil wets the probe, and causes difficulties when applying it to the probe. Ethylene glycol has a viscosity around five times greater than that of the silicon oil, and a moderate surface tension. Ethylene glycol is a hydrophilic, polar fluid where silicon oil is non-polar, hydrophobic material.

The hemispherical probe is constructed from a glass capillary tube with a diameter of 6.5 mm. Glass is chosen because its surface characteristics are well known. A set of standard conditions were adopted to make analysis easier. The volume of fluid used is 0.5 μL and the height of the probe from the surface of the substrate is 0.35 mm. These parameters remain constant for each fluid/substrate combination.

3.2 Theoretical relationship

When a given substrate is raised to the probe, the fluid on the tip of the probe contacts the substrate and creates a force of attraction between the probe and the substrate.

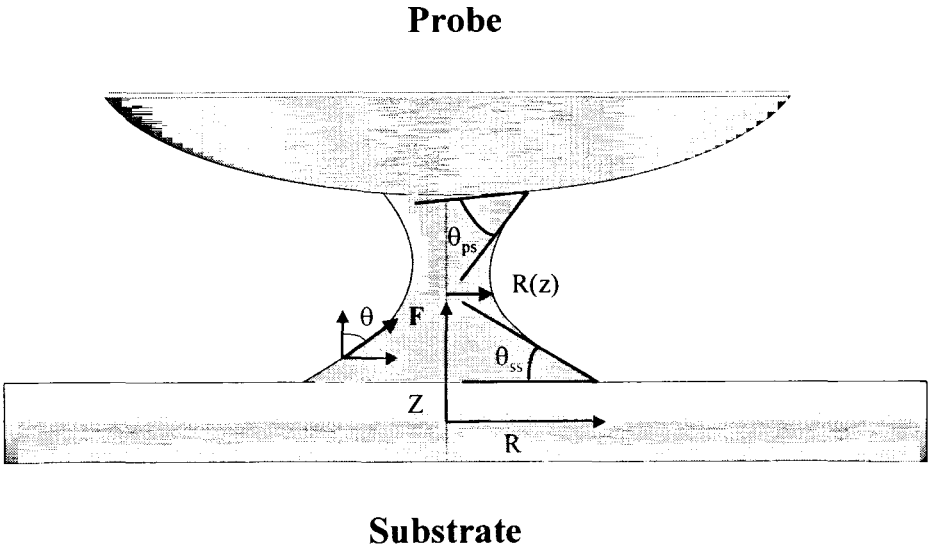

Figure 3.1: Fluid bridging between the glass probe and the porous substrate

For a static system with a non-porous substrate, Eq. (2.1) is valid. When the substrate is porous the fluid will be taken up by the substrate. At the present time scale of absorption, Eq. (2.1) should still be valid. Also the force parallel to the axis of the liquid bridge must be the same everywhere. The vertical component of the force is dependent on the curvature of the fluid bridge. Thus the relationship between the force at any axial position and the curvature is:

$$F = 2 \cdot \pi \cdot R(z) \cdot \sigma \cdot \cos\theta(z) \tag{3.1}$$

where F is the vertical force component, R(z) is the radius of the fluid column, σ is the surface tension of the fluid and $\theta(z)$ is the angle deviation from vertical. The shape of the fluid bridge is determined by the volume of fluid between the probe and the substrate in conjunction with the fluid-probe contact angle θ_{ps}, and the fluid-substrate contact angle θ_{ss}. By integrating the liquid bridge cross section over the height of the probe, we can calculate the volume of the fluid bridge V, as:

$$V = \int_0^{h_{ps}} (\pi \cdot R^2) dz \tag{3.2}$$

Now, the slope $\frac{dR}{dz}$ is equal to tan θ or:

$$dz = \frac{dR}{\tan\theta} = \frac{\cos\theta}{\sin\theta} d\left(\frac{F}{2 \cdot \pi \cdot \sigma \cdot \cos\theta}\right). \tag{3.3}$$

or

$$dz = \frac{F}{2 \cdot \pi \cdot \sigma \cdot \cos\theta} d\theta = R d\theta \tag{3.4}$$

Insertion of Eq. (3.1) and Eq. (3.4) in Eq. (3.2) one obtains:

$$V = \pi \int_{\theta_{ss}-90}^{90-\theta_{ps}} \left(\frac{F}{2 \cdot \pi \cdot \sigma \cdot \cos\theta}\right)^3 d\theta \tag{3.5}$$

After integrating Eq. (3.5), an expression relating the volume of the liquid bridge, to the contact angles and force is found as:

$$V = F^3 \cdot c_0 \tag{3.6}$$

where

$$c_0 = \frac{\sec(90-\theta_{ps}) \cdot \tan(90-\theta_{ps}) + \ln\left|\sec(90-\theta_{ps}) + \tan(90-\theta_{ps})\right| + \csc\theta_{ss} \cdot \cot\theta_{ss} - \ln\left|\csc\theta_{ss} - \cot\theta_{ss}\right|}{16 \cdot \pi^3 \cdot \sigma^3}.$$

Eq. (3.6) is a key result. However, contact angles are difficult to measure. To eliminate the need for visual contact angle measurement, we can estimate c_0 as $\frac{V}{F_{max}^{3}}$ where V and F_{max}, the initial volume of the fluid drop and the maximum force, are both measured experimentally.

Taking the derivative of Eq. (3.6) with respect to time t, we see the resulting fluid uptake rate:

$$\frac{dV}{dt} = 3 \cdot c_0 \cdot F^2 \frac{dF}{dt} \tag{3.7}$$

Equation 3.7 can be rewritten as:

$$-\frac{dF}{dt} = \frac{-\frac{dV}{dt}}{3 \cdot c_0 \cdot F^2} \tag{3.8}$$

This is a key relationship to understanding how the recorded force changes with a fluid uptake rate.

The porous substrates of interest are thin compared to the volume of the fluid. Therefore the substrate thickness below the liquid footprint is filled rapidly and the measured response is radial spreading. If the footprint of the liquid column is fixed, circular, and there is only radial spreading, we can simplify the analysis. For the thin coating layers we assume radial spreading. This is a good assumption because most samples have thin porous structures that are saturated upon contact as depicted in Figure 3.2.

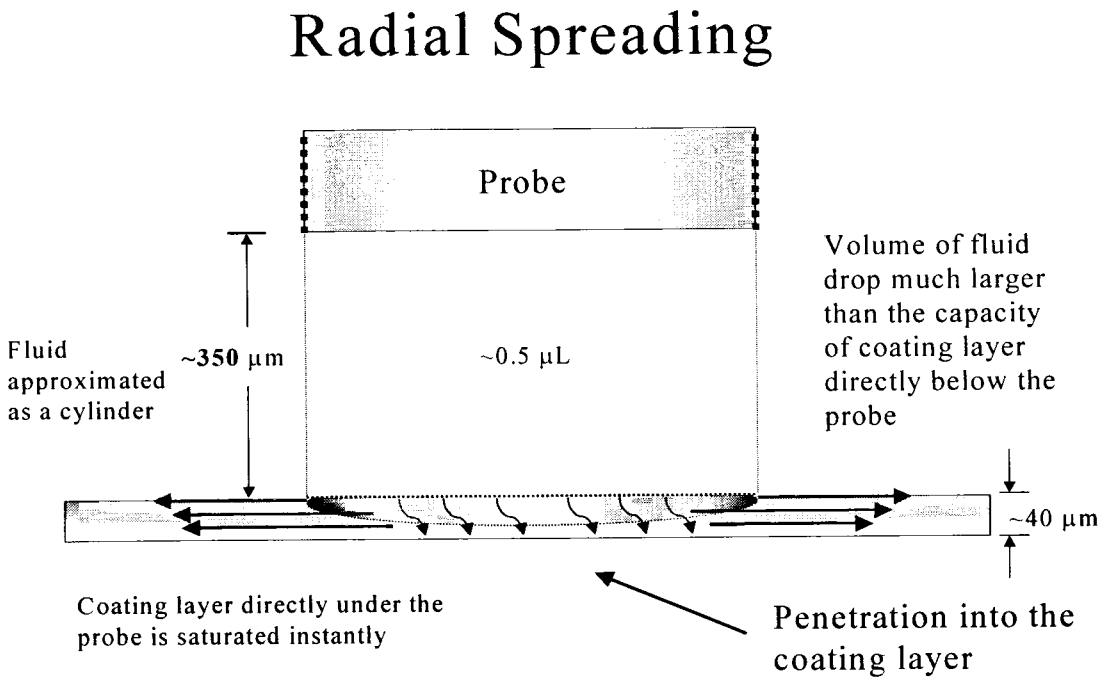

Figure 3.2: Fluid instantaneously saturates coating then slowly spreads radially.

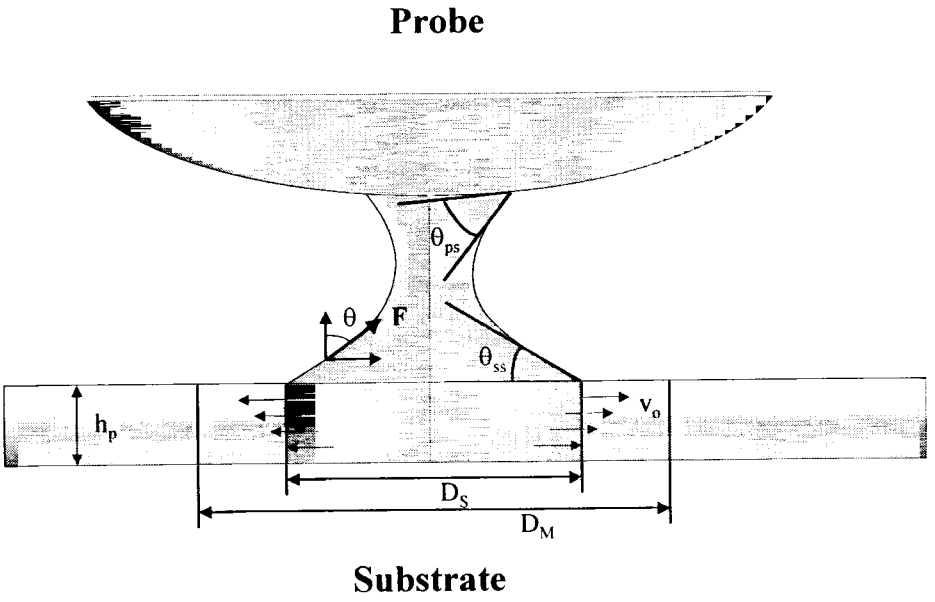

Figure 3.3: Diffusive flow through a porous substrate.

When fluid is taken up in the radial direction, the volume rate of change is:

$$\frac{dV}{dt} = \pi \cdot D_S \cdot h_p \cdot \frac{\varepsilon}{2} \cdot \frac{d(D_M - D_S)}{dt} \tag{3.10}$$

also

$$\frac{dV}{dt} = v_0 \cdot \pi \cdot D_S \cdot h_p \tag{3.11}$$

where D_S is the diameter of the footprint on the substrate, D_M is the saturation front, ε is the void fraction, h_p is the thickness of the porous layer, and v_0 is the fluid velocity at the edge of the footprint in the porous media. This velocity v_0 should follow the Blake-Kozeny equation. In the radial direction this is:

$$v_0 = \frac{2 \cdot \Delta p}{(D_M - D_S)} \cdot \frac{d_p^{\,2}}{150 \cdot \eta} \cdot \frac{\varepsilon^3}{(1-\varepsilon)^2} \tag{3.12}$$

where d_p is the particle diameter inside the porous layer, D_M is the diameter of the liquid interface in the radial direction on the porous material, Δp is the pressure driving force to capillary effects, and η is the viscosity of the fluid. By setting Eq. (3.10) equal to Eq. (3.11) the result is that:

$$(D_M - D_S) = \left(\frac{8}{150} \cdot \frac{\Delta p}{\eta}\right)^{\frac{1}{2}} \cdot \frac{d_p \cdot \varepsilon}{(1-\varepsilon)} \cdot \sqrt{t}\,. \tag{3.13}$$

According to the Young-Laplace relationship the pressure difference Δp that drive the flow into the pores is:

$$\Delta p = \frac{2 \cdot \sigma \cdot \cos\theta_{ss}}{r_p}. \tag{3.14}$$

where r_p is the equivalent pore radius of the porous substrate. By inserting Eq. (3.14) into Eq. (3.10) and (3.13) the combined result is:

$$\frac{dV}{dt} = \pi \cdot D_S \cdot h_p \cdot \frac{\varepsilon}{4}\left(\frac{8}{150} \cdot \frac{\Delta p}{\eta}\right)^{\frac{1}{2}} \cdot \frac{d_p \cdot \varepsilon}{(1-\varepsilon)} \cdot \frac{1}{\sqrt{t}}. \tag{3.15}$$

By inserting Eq. (3.15) into Eq. (3.8) and rearranging terms, we get:

$$\frac{dF}{dt} = -\frac{\pi \cdot D_S \cdot h_p}{6 \cdot c_0 \cdot F^2} \cdot \frac{d_p \cdot \varepsilon^2}{(1-\varepsilon)} \cdot \left(\frac{2 \cdot \Delta p}{150 \cdot \eta}\right)^{\frac{1}{2}} \cdot d(\sqrt{t}). \tag{3.16}$$

After integrating, rearranging, and solving for the force, the resulting relationship is:

$$F_{\max}{}^3 - F_t{}^3 = \frac{\pi \cdot D_S \cdot h_p \cdot d_p \cdot \varepsilon^2}{c_0(1-\varepsilon)}\left(\frac{2 \cdot \Delta p}{150 \cdot \eta}\right)^{\frac{1}{2}} \cdot \sqrt{t - t_{\max}} \tag{3.17}$$

or

$$F_t = \sqrt[3]{F_{\max}{}^3 - \frac{\pi \cdot D_S \cdot h_p \cdot d_p \cdot \varepsilon^2}{c_0(1-\varepsilon)}\left(\frac{2 \cdot \Delta p}{150 \cdot \eta}\right)^{\frac{1}{2}} \cdot \sqrt{t - t_{\max}}}. \tag{3.18}$$

where F_{max} is the maximum force and t_{max} is the time at the maximum force. If the theoretical model is accurate, then Equation 3.18 should predict the force that the fluid applies to the probe as a function of time.

If all of our assumptions are correct, when $F_{\max}{}^3 - F_t{}^3$ vs $\sqrt{t - t_{\max}}$ is plotted, the slope will be:

$$slope = \frac{\pi \cdot D_{SS_n} \cdot h_p \cdot d_p \cdot \varepsilon^2}{c_0(1-\varepsilon)}\left(\frac{2 \cdot \Delta p}{150 \cdot \eta}\right)^{\frac{1}{2}}. \tag{3.19}$$

3.3 Typical force-time results

Initial testing of model porous media is achieved by testing samples that have a controlled void fraction. Two plastic pigment systems with 10 and 40 pph latex were used with water. Fig. 3.4 and 3.5 show the results.

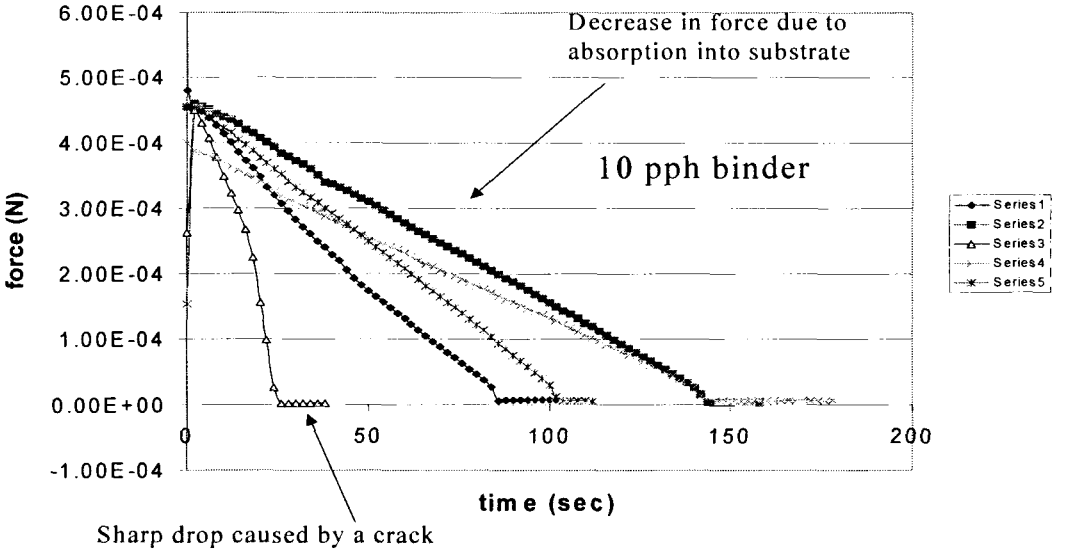

Figure 3.4: Plastic pigment 10 pph binder with sharp force decrease.

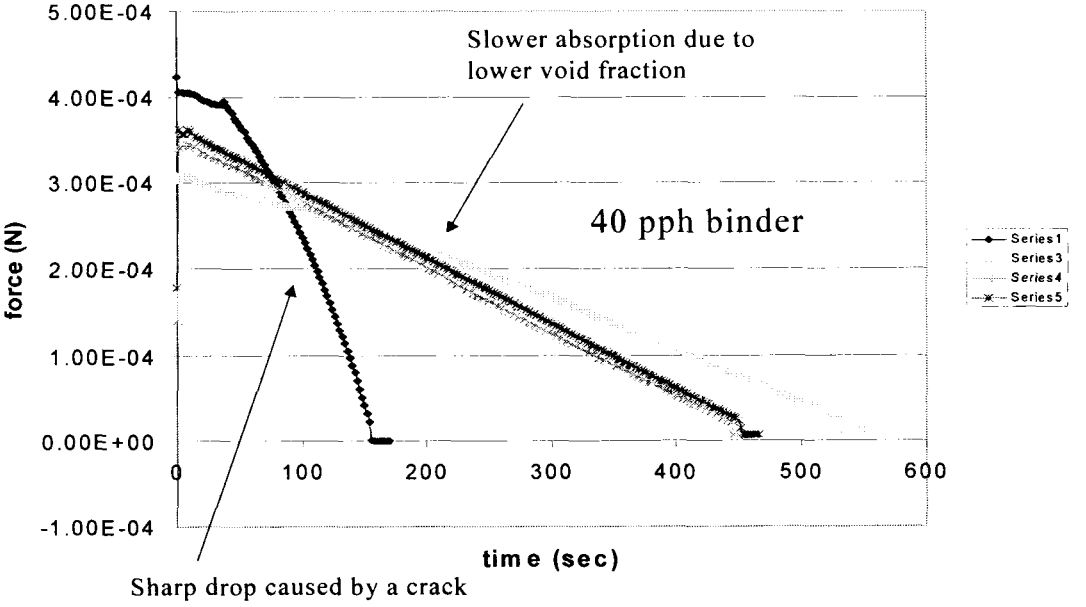

Figure 3.5: Plastic pigment 40 pph binder with gradual force decrease.

For all of the porous substrates, a peak force is seen as the fluid contacts the surface, followed by a decrease in force as the fluid absorbs and/or evaporates. Notice the time scale difference between the two samples with different binder concentrations. The 10 pph binder system is known to take up water about three times as fast as the 40 pph system as seen by Bousfield et al. (2000). This difference is close to the difference in the time for the force signal to return to zero. The silicon oil systems take about five times longer for the force to return to zero (for the fluid bridge to break). This is very close to what would be expected based on absorption as the controlling mechanism for the force decrease.

3.4 Comparison with model

To compare with the model, standard conditions are established. A volume of 0.5 micro-liters is used as a basis fluid volume and 0.35 mm is used as a basis probe height (distance from the probe to the substrate). The seven substrates seen in Table 3.1 were tested with the three model fluids. For each fluid and substrate combination, three runs were recorded.

Sample C is chosen as an example in this discussion. Figure 3.5 shows a typical set of raw force/time data at the standard conditions. From one location to another, a repeatable result is obtained. The time for the liquid bridge to brake and the average and standard deviation of each set of three runs are calculated. The average force time curve are then plotted against the theoretical force/time prediction. Figures 3.6 thru 3.8 display the model results of Eq. (3.17) with experimental results for substrate C and the three fluids. The fluid and sample properties in Tables 3.1 and 3.2 are used. The comparison is good for all three fluids, including the shape of the curve. The theory over predicts the force at long times for the silicon oil.

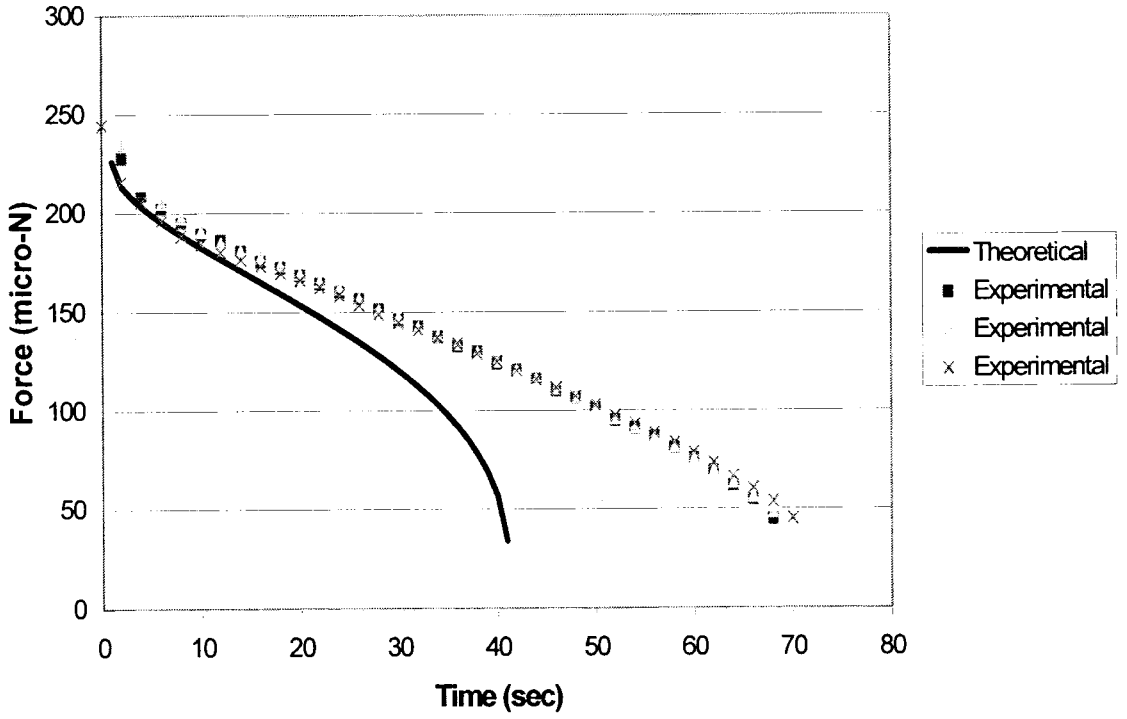

Figure 3.6: Theoretical prediction and experimental data for water on sample C.

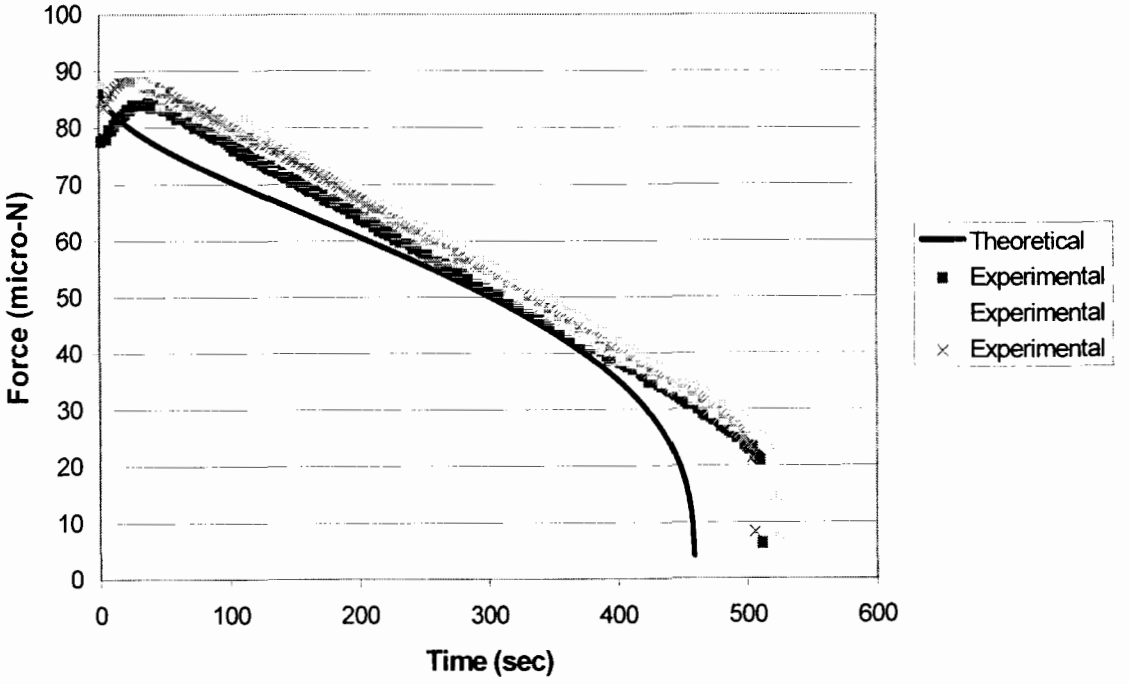

Figure 3.7: Theoretical and experimental data for silicon oil on sample C.

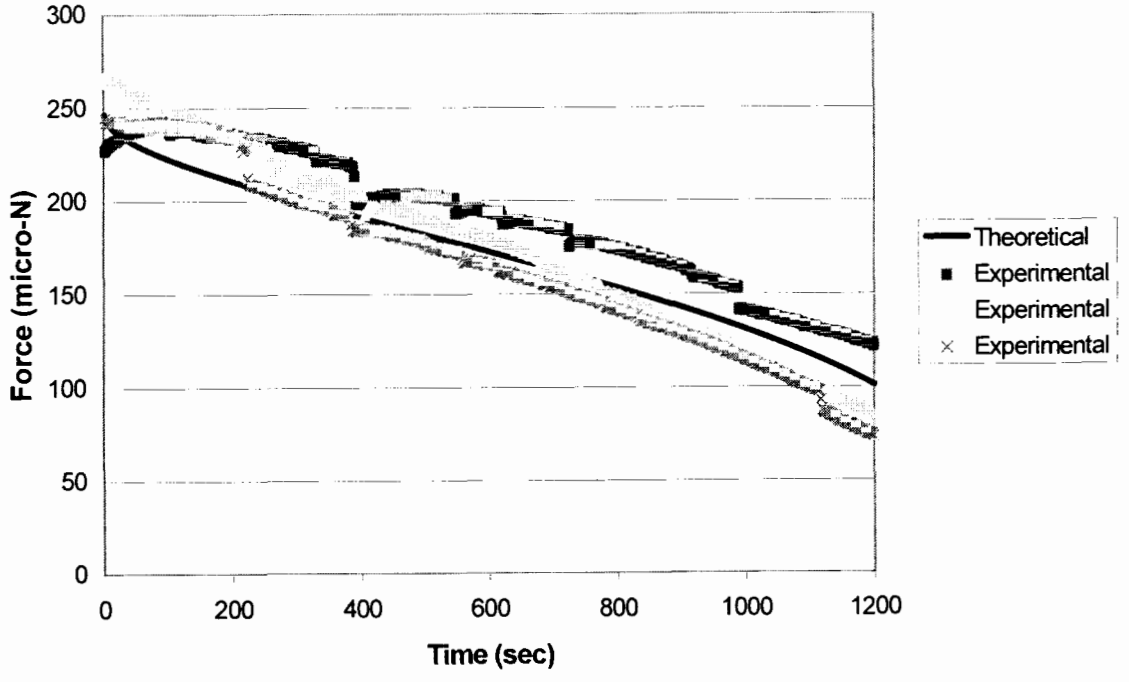

Figure 3.8: Theoretical and experimental data for ethylene glycol on sample C.

If we plot $F_{max}{}^3 - F_t^3$ vs $\sqrt{t - t_{max}}$ we should obtain a straight line whose slope is given by Eq. (3.10). The slope of the experimental data is determined by a least squares best fit, as shown in Figure 3.10. The best fit line must be forced through zero because the model demands it.

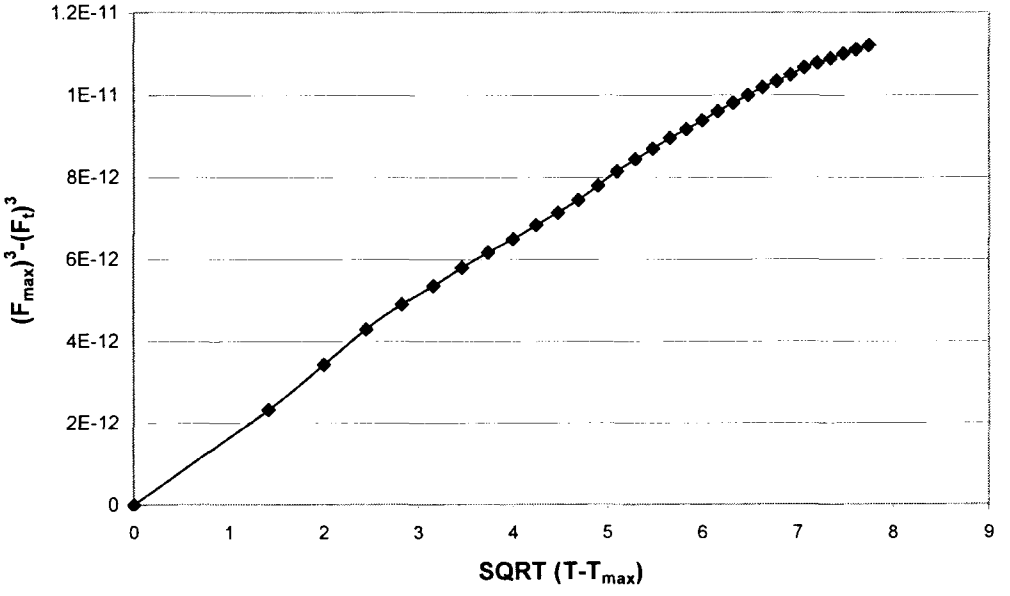

Figure 3.9: Results of applying theoretical relationship to experimental force/time data for water on 10 pph sample.

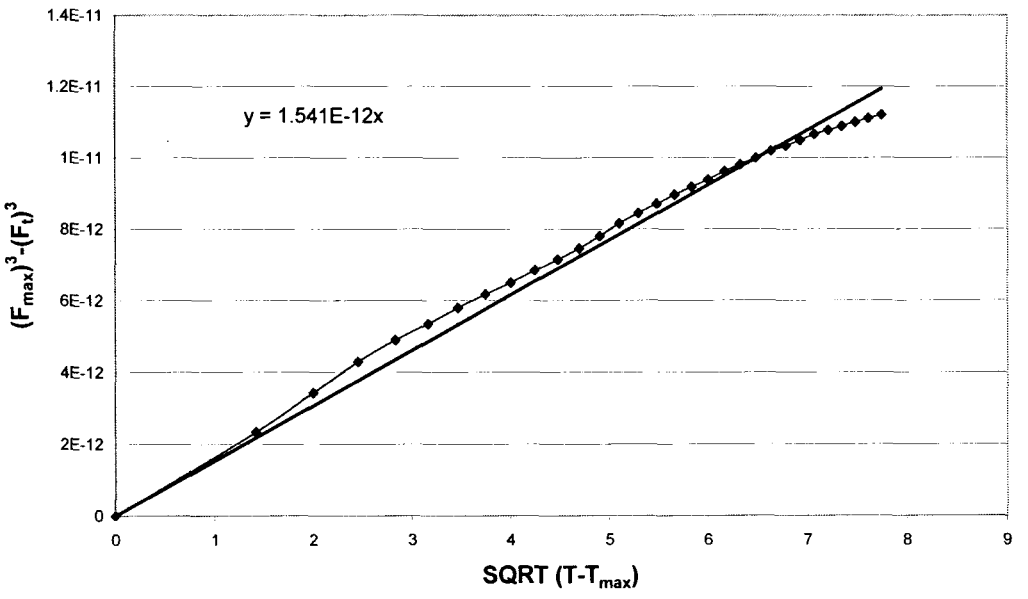

Figure 3.10: Slope of force cubed versus square root of time data for water on 10 pph sample.

Knowing the slope of this line we are then able to compare it to the slope derived by the theoretical model. The results of the experimental slopes from all seven substrates are plotted versus the theoretically calculated slopes.

Not all of the data fit the theoretical model as well as Media C. The fluid/probe interaction of Media A, a commercial ink jet media, was not predicted by the model. The discrepancy is though to be due to structure and porosity of the individual coating particles themselves. The experimental data and the theoretical prediction of the force/time curve for the three fluids are seen in Figures 3.11 thru 3.13.

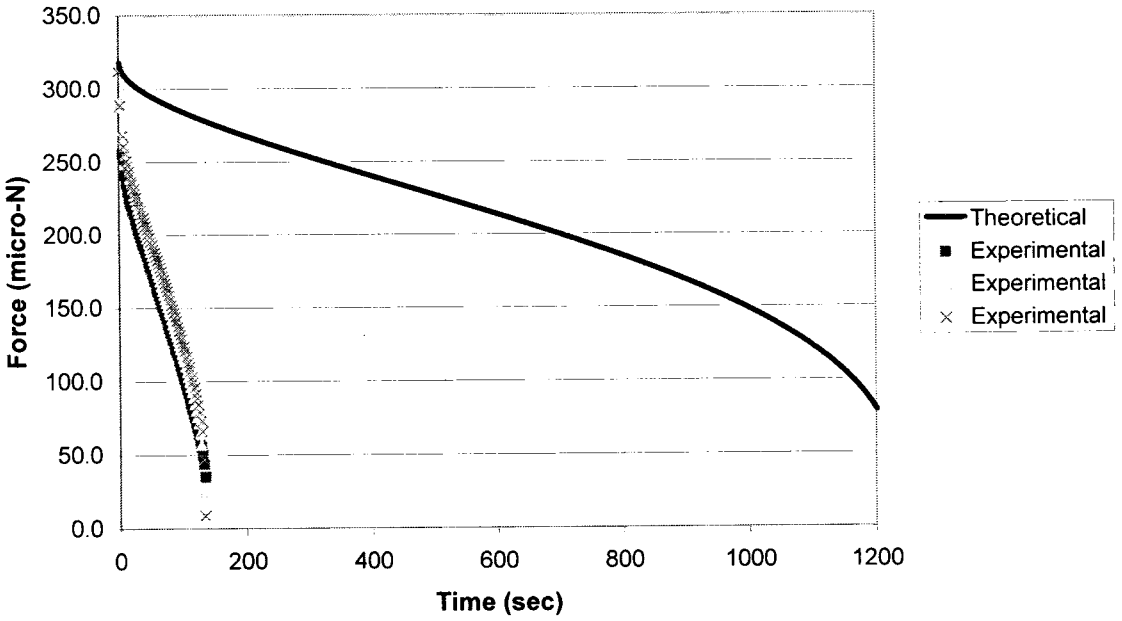

Figure 3.11: Experimental data and theoretical prediction for water on Media A.

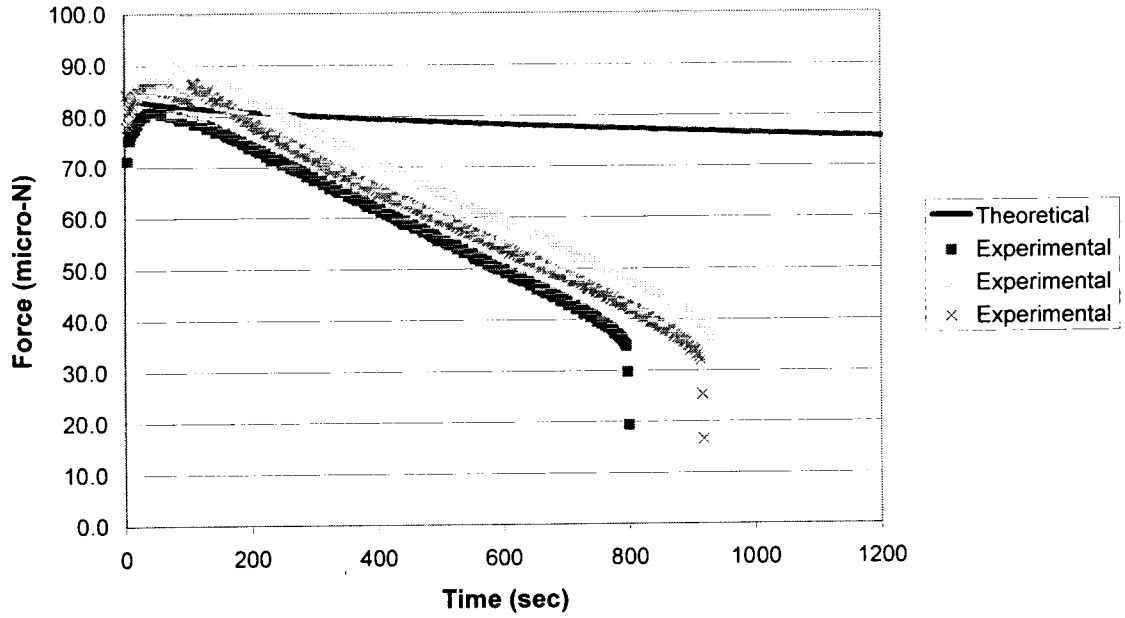

Figure 3.12: Experimental data and theoretical prediction for silicon oil on Media A.

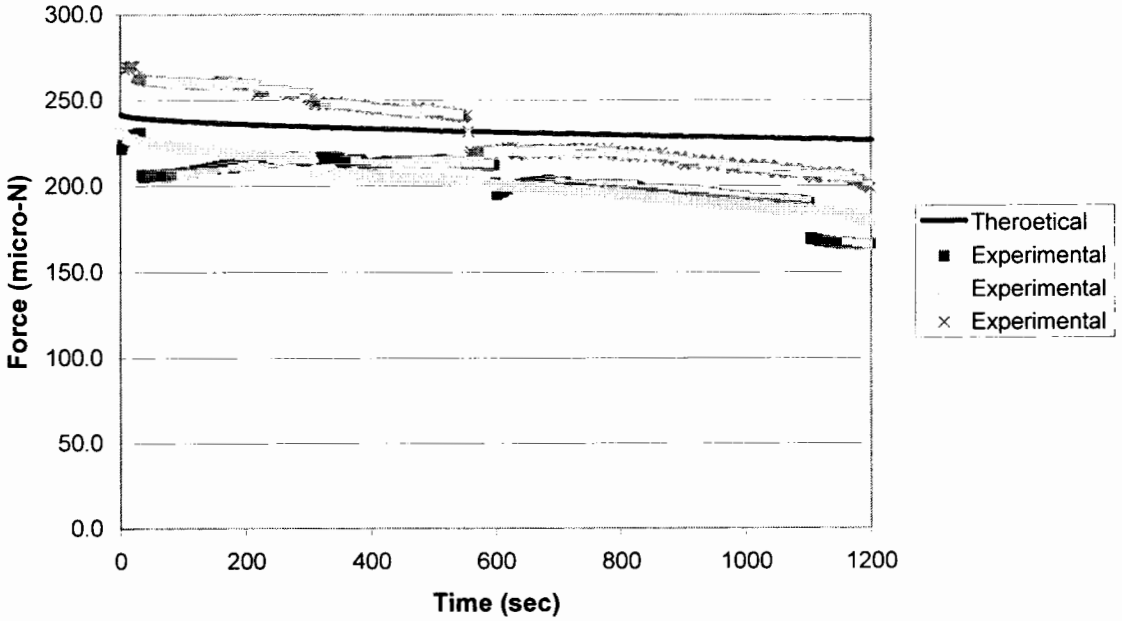

Figure 3.13: Plot of experimental data and theoretical prediction of ethylene glycol on Media A.

For the experimental data, the propagation of error from the standard deviation is calculated to determine error bars associated with each data point. For the theoretical model, a complete error analysis is completed in order to quantify the propagation of error due to the inaccuracy of measured parameters (see Appendix C). Figures 3.14 thru 3.16 illustrate the results of the seven substrates with each of the three given fluids.

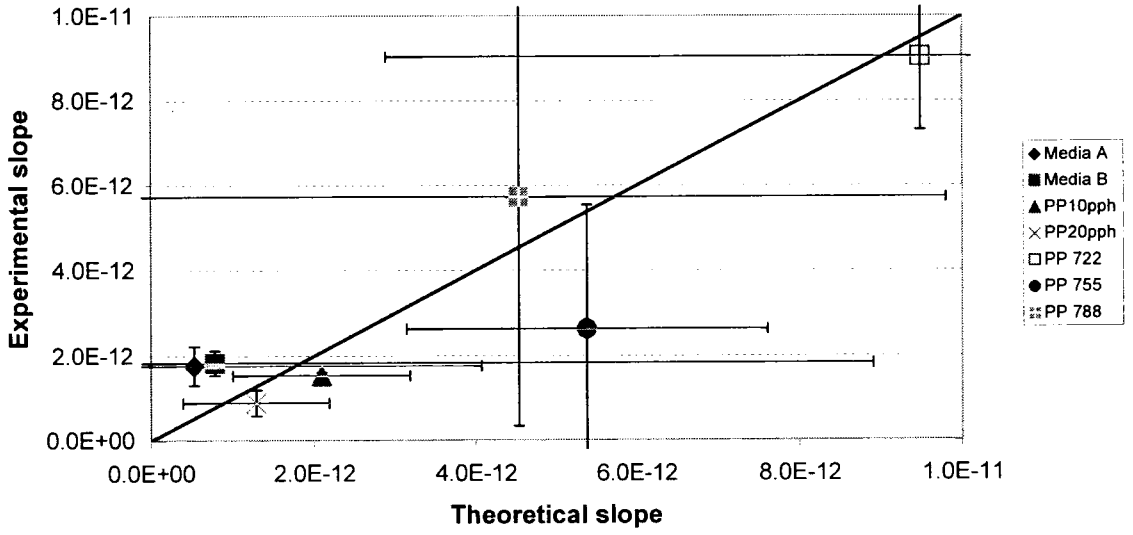

Figure 3.14: Forty-five degree plot of the model porous substrates with water.

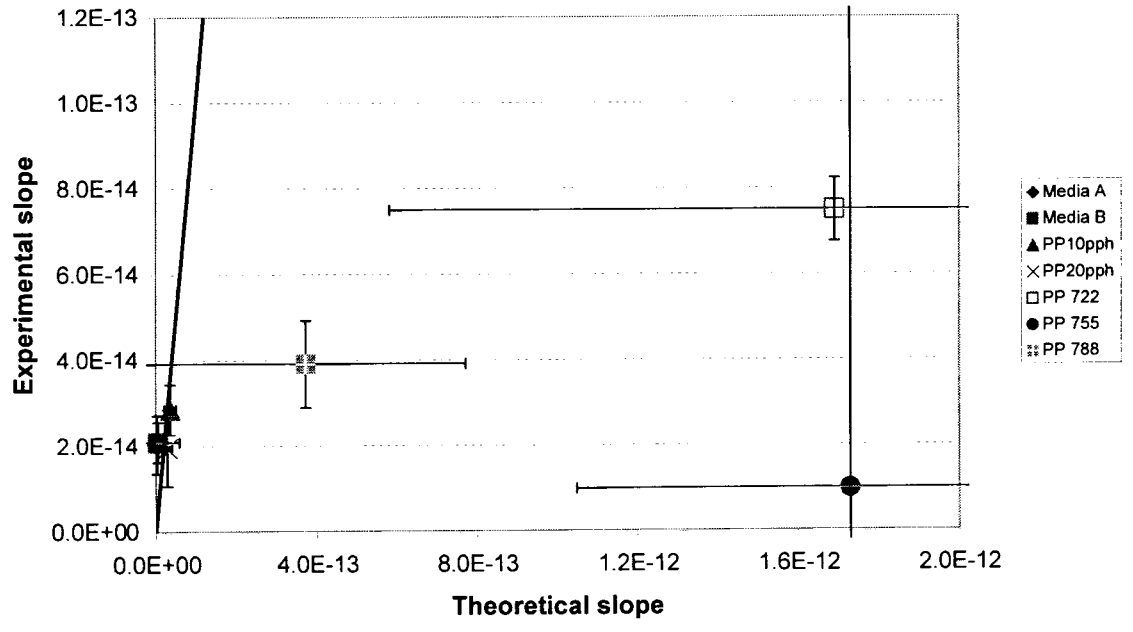

Figure 3.15: Forty-five degree plot of model porous substrates with silicon oil.

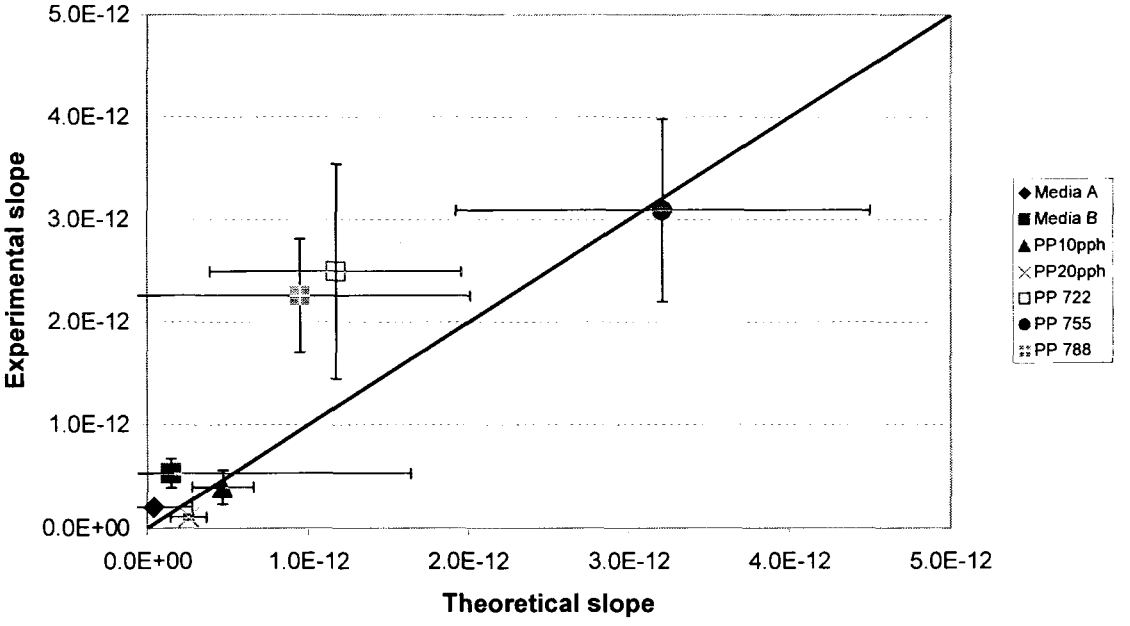

Figure 3.16: Forty-five degree plot of seven model porous substrates with ethylene glycol.

The 45 degree plots serve as a way to determine how well the actual experimental data matches the theoretical model. The commercial inkjet media is not as simple randomly packed spheres.

3.5 Discussion

The theoretical model makes a number of assumptions. The model assumes no Z-directional penetration, but this should be good because most samples have thin porous structures that are saturated upon contact. The model assumes that the footprint of the column of fluid is circular and fixed throughout as penetration proceeds. From video images, the footprint may change as much as 10%. This change is not enough to explain

the differences. The flow in the radial direction is based on the Blake-Kozeny equation. This description can be wrong, especially if the porous media has dead ends, or unusual pore shapes. The model assumes equal radial spreading in all directions, but some substrates may not act in this manner. The driving force for the flow is calculated using a dominant pore size. Again, complex pore structures may cause this to be incorrect.

In view of how well we know the properties of the substrates and the assumptions of the model, the comparison with the experimental results is good. The slopes can vary by a factor of 100. The shapes of the curves, for the most part, are duplicated. Considering the range of the fluids and substrates, the results are good.

3.6 Force vs. contact angle

The minimum radius of the fluid determines the magnitude of the force between the probe and the substrate. When considering the geometry of the fluid bridge, we conclude that when the contact angle of the fluid with the substrate is at 90^{o}, r_{min} is at a maximum. For contact angles greater or less than 90^{o}, r_{min} will be lower and result in a lower force. The contact angle between the fluid and the substrate is a direct result of the surface tension of the fluid and the surface energy of the substrate. When the peak force is plotted versus the contact angle for the porous substrates as in Fig. 3.17, this basic trend is observed. For small contact angles the force is quite sensitive to the contact angle.

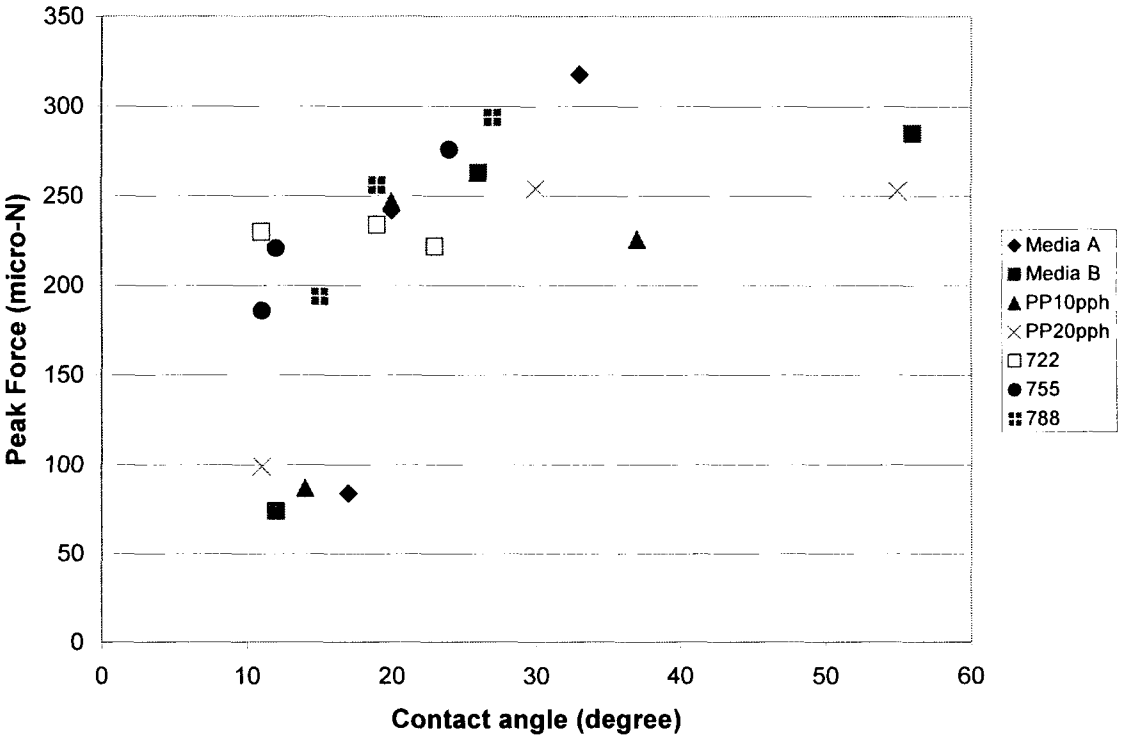

Figure 3.17: Plot of peak force vs. contact angle for water, silicon oil, and ethylene glycol on the seven -porous substrates at a gap of 0.35 mm.

3.7 Conclusions

Porous substrates give an early peak force followed by a decrease. Decrease is related to the rate of absorption. A model is developed based on radial capillary flow to describe experimental results. While not perfect, the model does a good job at predicting experimental results. The peak force is linked to the surface chemistry and surface energy of the substrate. Maximum force will be seen when the contact angle between the fluid and the substrate is 90°. Contact angles greater or less than 90° with the substrate will result in a lower peak force.

Chapter 4: Swellable Substrates

A swellable substrate is defined here as a substrate that takes up fluid due to diffusion. This fluid uptake mechanism is in contrast to the last chapter that focused on capillary absorption. The goal of this chapter is to examine the results of the experimental technique with swellable substrates. In light of relationships drawn from the fluid interactions with porous substrates, we can understand the general behavior in this case. A series of tests were done on cellophane and two ink jet media. Standard conditions defined in Chapter 3 are used in testing swellable substrates.

4.1 Materials

A cellophane film and two photo based inkjet media are used as three models of swellable substrates. The cellophane has a thickness of 0.06 mm and absorbs about 45 g/m^2 of water. The two glossy inkjet media C and D are produced for premium printing and have numbers C6058A and HPC5982A, respectively. These media are made with a layer of a water swellable polymer film. Media C is comprised of a paper substrate with a thin polymer coating. Media D is comprised of a polymer coated plastic sheet. The same probe fluids of water, silicon oil, and ethylene glycol are used to test these samples. The fluid properties are reported in Chapter 3.

Table 4.1 summarizes the swellable substrate properties. The contact angle is obtained as described in chapter 3. The absorption capacity is obtained by weighing a sample,

soaking it in the test fluid for 24 hours, removing the excess fluid, and weighing the sample again. In some cases, the coating comes off the substrate, and the absorption capacity is suspect.

contact angles in degrees @ 0.1 sec

	Cellophane	Media C	Media D
Water	38	60	92
Silicon Oil	10	17	9
Ethylene Glycol	27	30	78

absorbtion gm/m2

	Cellophane	Media C	Media D
Water	44.8	- *	10.96 *
Silicon Oil	0.0	42.8	2.3
Ethylene Glycol	39.6	- *	48.6

* dissolving problem

Table 4.1: Swellable substrate properties.

4.2 Results

Force responses depend on the probe fluid used to analyze the substrate. Figures 4.1 through 4.3 show the force time response of the three fluids on cellophane. For water, the force decreases with time and the liquid bridge breaks around 450 s. However, silicon oil and ethylene glycol, the force does not show a decrease but a small increase or a steady force. The decrease with water is expected because cellophane absorbs water. This would decrease the liquid bridge volume and decrease the force. Cellophane is not expected to absorb the silicon oil or the ethylene glycol, but on absorption test, cellophane did seem to absorb ethylene glycol for a contact time of approximately 24 hours.

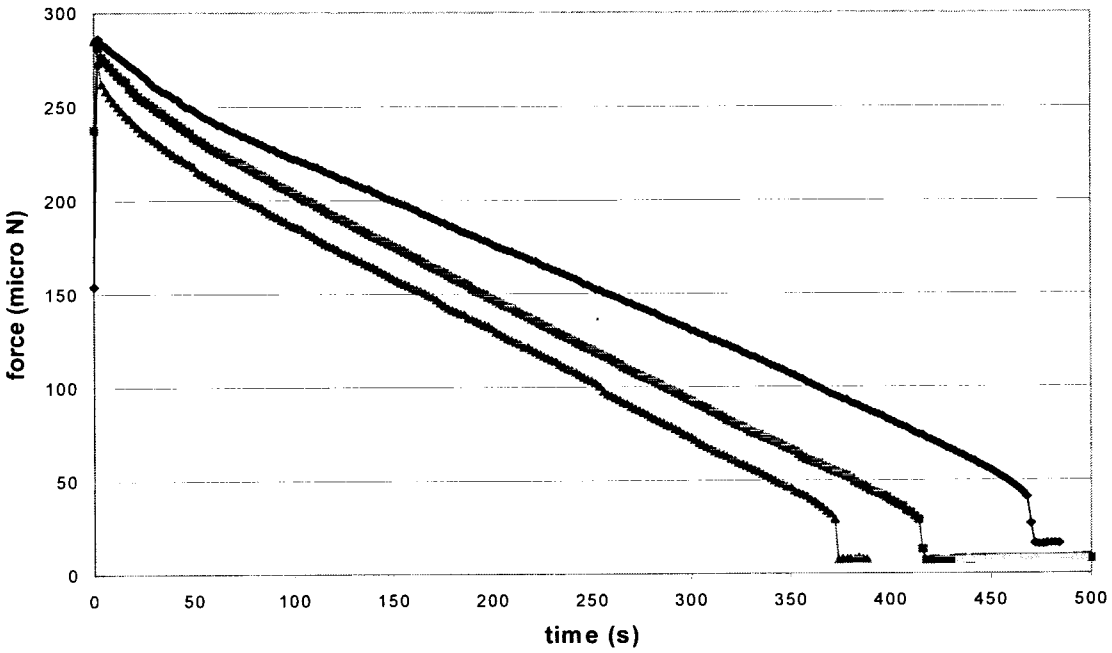

Figure 4.1: Experimental force/time response of water on cellophane. The different curves are different locations.

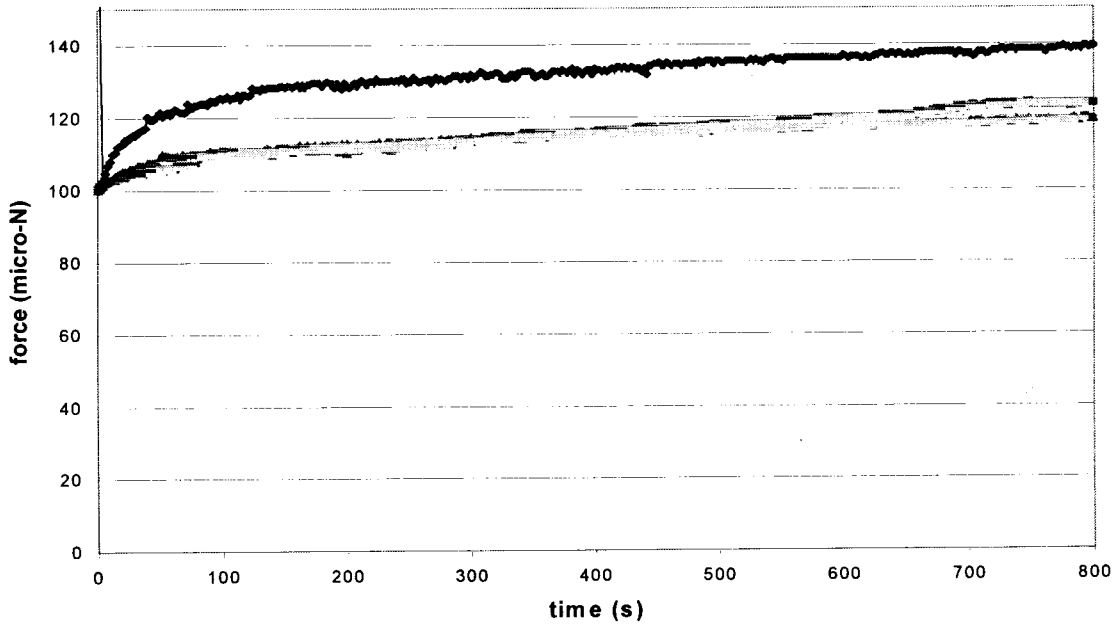

Figure 4.2: Experimental force/time response of silicon oil on cellophane.

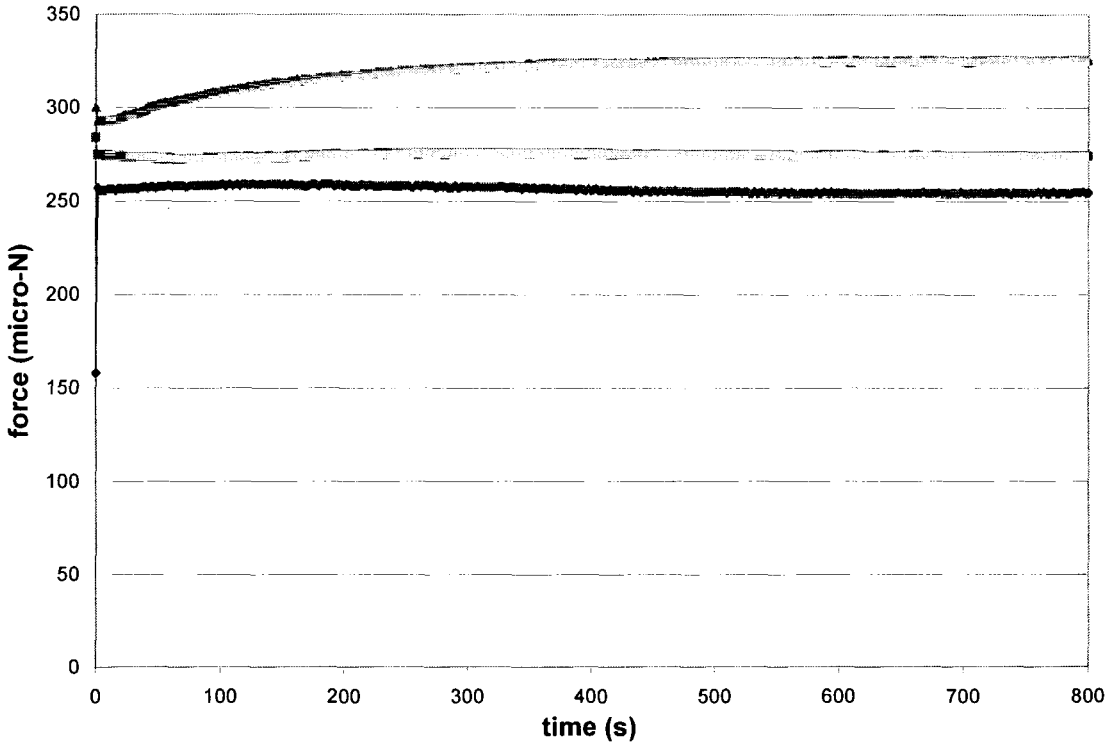

Figure 4.3: Experimental force/time response of ethylene glycol on cellophane.

The time scale for cellophane to absorb water should be compared to the time required for evaporation. Actually, the time to evaporate a drop of water on glass is approximately 300 s. Therefore, it is difficult to understand why on cellophane, the time for the liquid bridge to break is longer.

When silicon oil is applied to the cellophane the force tends to steadily increase over time. An increase in force means that there is an increase in the minimum radius of the fluid column. There are a few possible explanations to account for this behavior. One possibility is that the substrate is swelling in the z-direction so as to decrease the distance between the probe and the substrate and increase the radius of the column. Another

possible explanation for an increase in force is that the fluid is receding on the substrate, thus increasing the minimum radius. This explanation seems unlikely because a substrate is not likely two dewet over such a long period of time. If the surface energy is high enough to cause the molecules in the fluid to have a higher attraction for themselves rather than the substrate, the congregation of fluid molecules would happen quickly. Another possible explanation is that the footprint of the silicon oil on the cellophane is fixed and the probe is dewetting due to gravitational forces thus increasing the amount of fluid in the column and increasing the minimum radius. This phenomenon is illustrated in Figure 4.4.

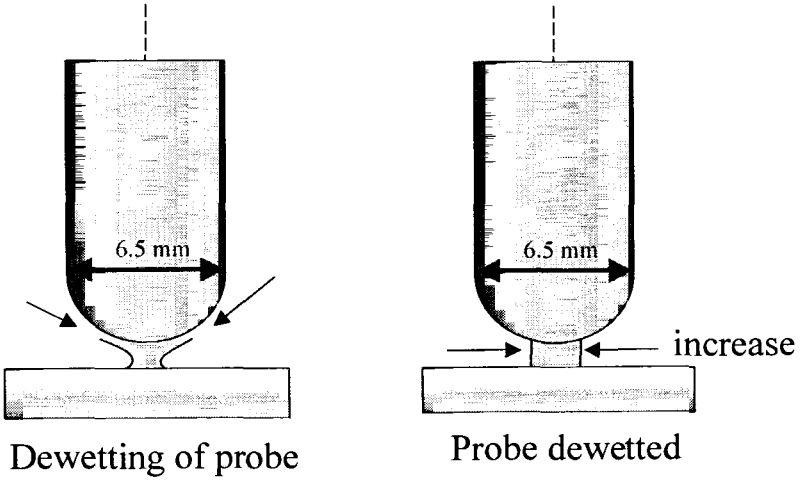

Figure 4.4: Minimum radius of fluid bridge increases as probe dewetts

The response obtained with ethylene glycol on cellophane is flat. For the most part, once the system has come to equilibrium, the force does not change over time. This shows the fluid is neither absorbing, spreading, nor evaporating.

Figures 4.5-4.7 show the force time response of the three fluids on media C. The response with water shows a similar result to that of cellophane, although this data has a more linear slope than that of cellophane. We can assume that most of the water applied to the probe evaporates. This is verified as water applied to a glass substrate gives similar results. The response for silicon oil on Media C is similar to that of cellophane. The same trend of increasing force is seen. The peak force of silicon oil on Media C is also lower in magnitude than that of cellophane. The absorption data from Table 4.1 shows that Media C absorbs a significant amount of silicon oil. This result is due to the fact that Media C has a paper base sheet, which absorbs the oil.

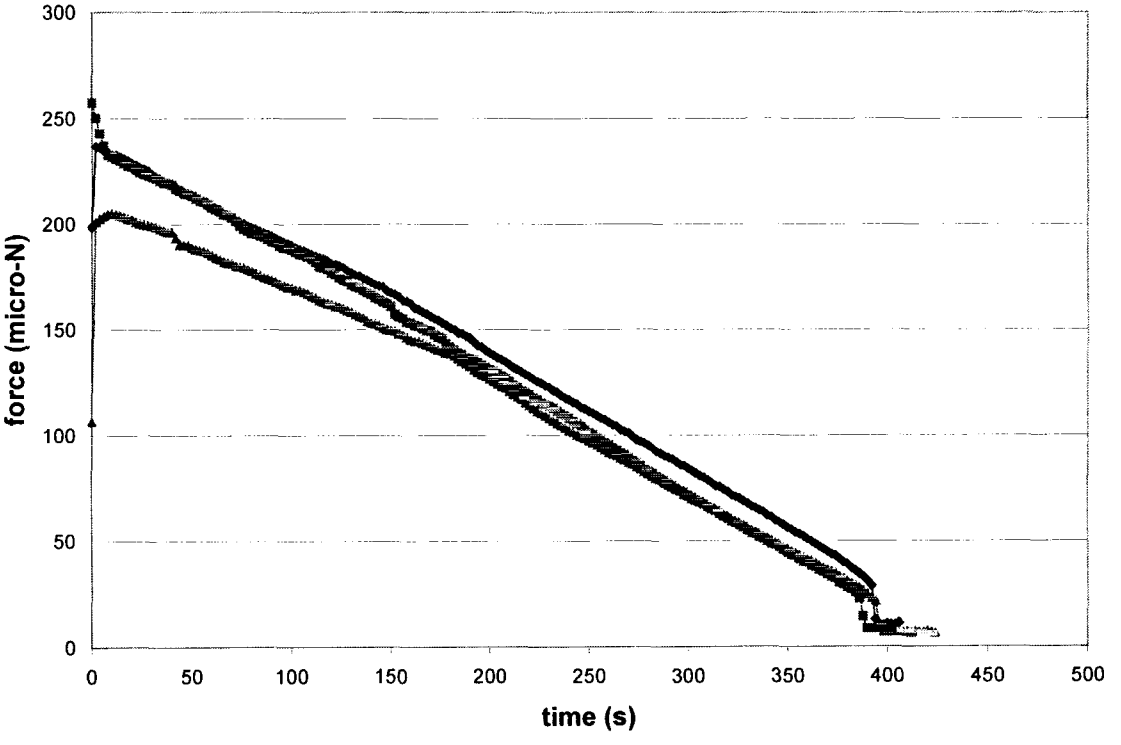

Figure 4.5: Experimental force/time response of water on Media C.

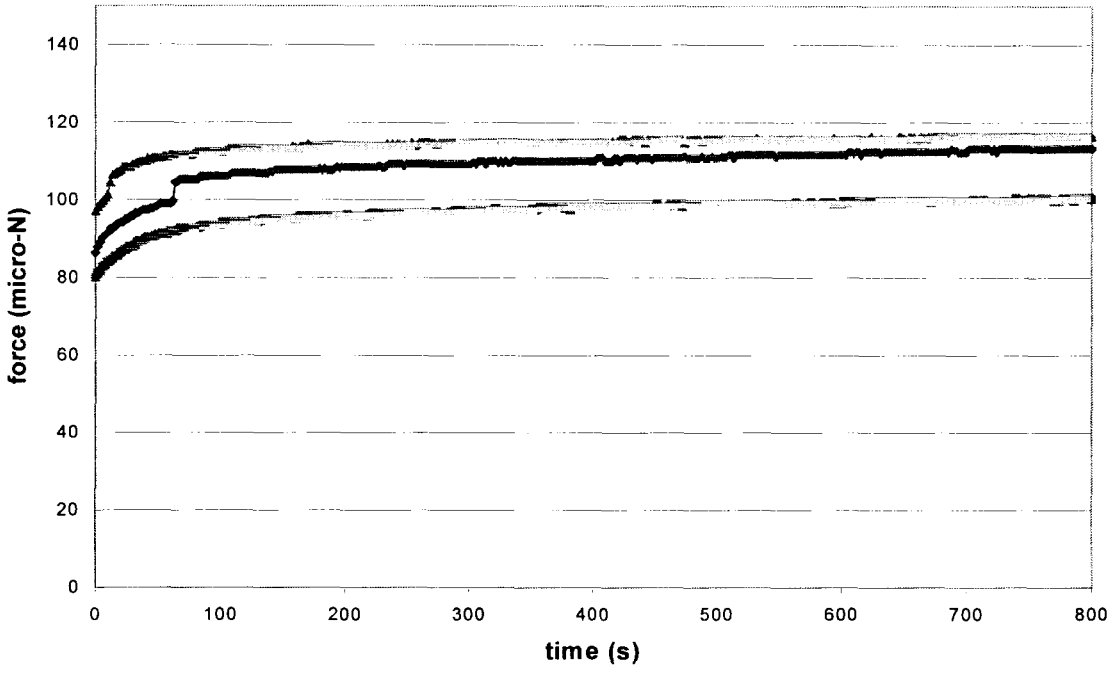

Figure 4.6: Experimental force/time response of silicon oil on Media C.

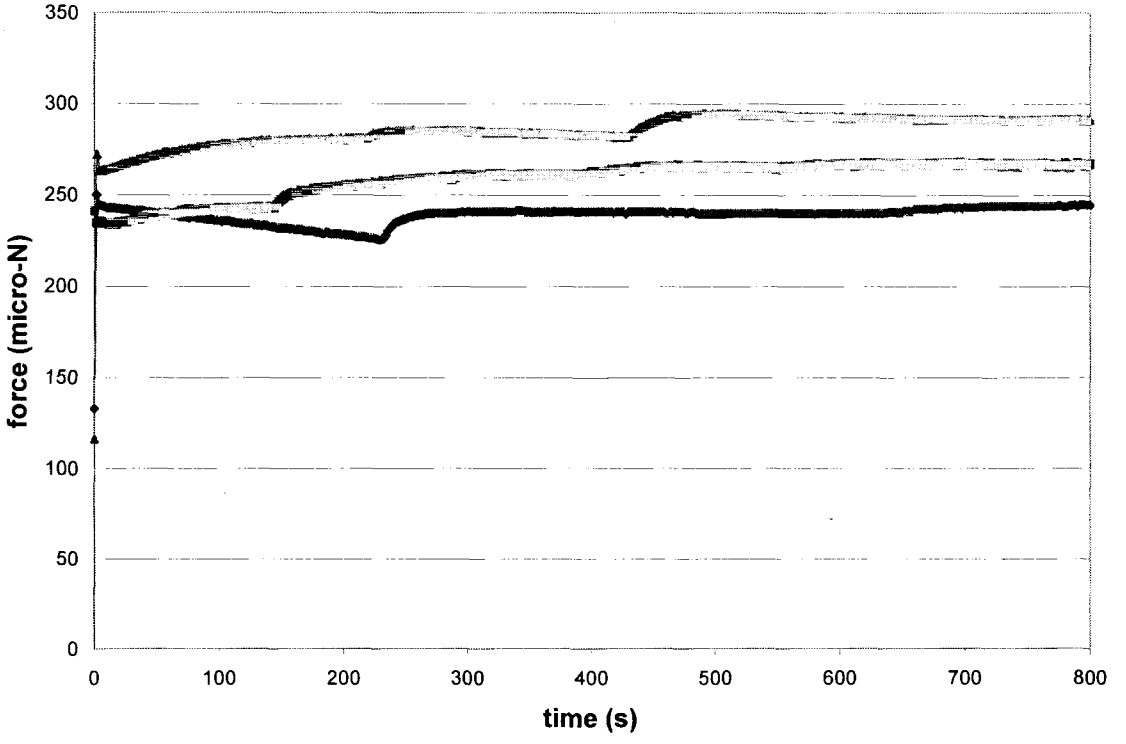

Figure 4.7: Experimental force/time response of ethylene glycol on Media C.

The response of ethylene glycol on Media C is similar the response on cellophane. When the system comes to steady state the force remains essentially constant. There is some interesting behavior that seems to be present in the force/time curves for ethylene glycol on Media C. There is a situation that is taking place at a certain instant where the force suddenly increases. This small increase seems to occur once at various times. The possible cause is not clear at present.

Figures 4.8 thru 4.10 show the force time response of the three fluids on Media D. The response of water on media D is different from the responses of the other two substrates. One difference is that there is a slight rounding of the initial part of the curve. This can also be explained by the contact angle of the fluid with the substrate being greater than 90 degrees and slowly decreasing as the substrate wets. Visual analysis confirms this mechanism and is discussed later.

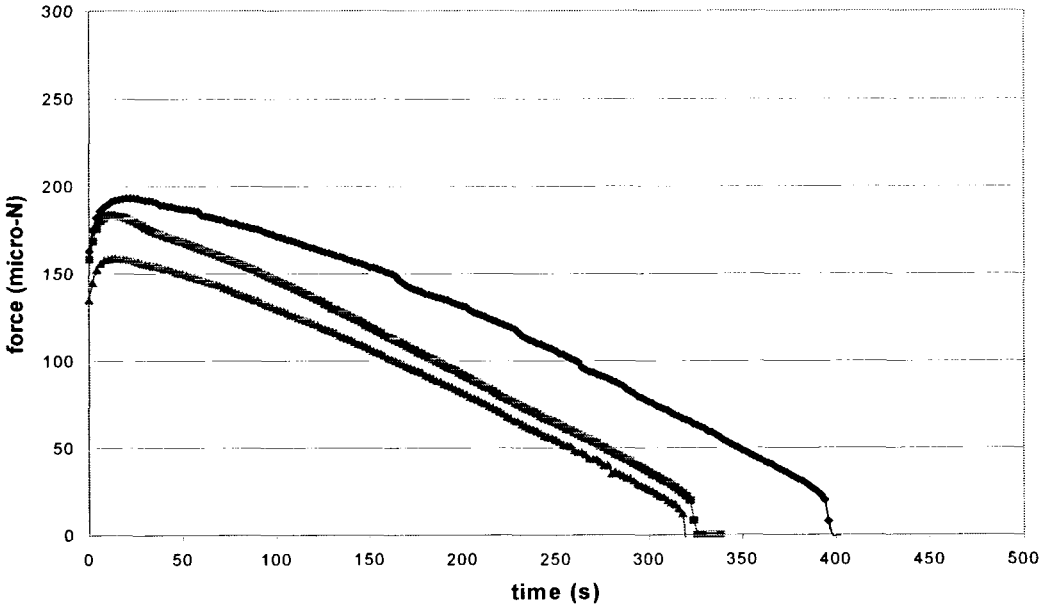

Figure 4.8: Experimental force/time response of water on Media D.

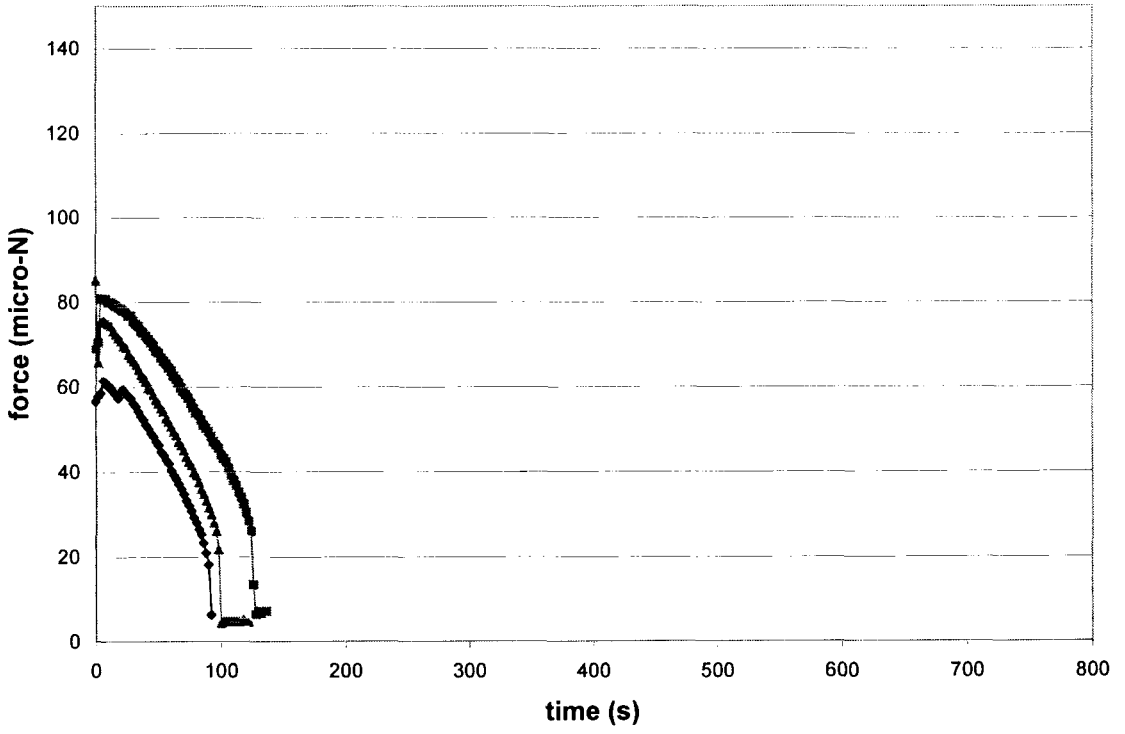

Figure 4.9: Experimental force/time response of silicon oil on Media D.

Silicon oil on media D is quite different on cellophane and media C. The magnitude of the force is lower in comparison to the other two but the striking difference is that the force drops off very rapidly. This is most likely due to the low surface energy of the substrate. Silicon oil has a low contact angle and spreads out over the sample. The wetting force of the substrate is larger than the wetting force of the probe.

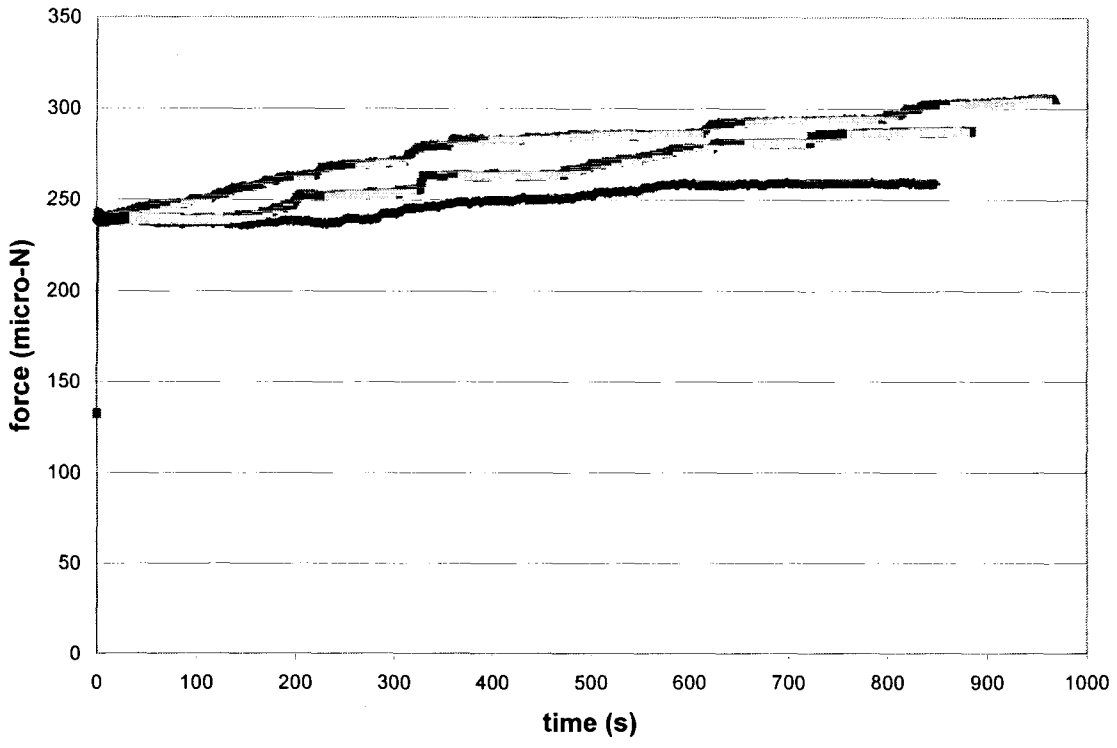

Figure 4.10: Experimental force/time response of ethylene glycol on Media D.

Media D with ethylene glycol shows a number of force jumps similar to the single force jump on media C. The sudden jumps in force repeat. The force continues to increase over time.

4.3 Increase in force

With porous substrates, we had only seen the force of the fluid on the probe decrease after contacting the substrate. However, when water is applied to swellable substrates, the force sometimes increases to a maximum and then decreases, as in Fig. 4.10. From visual observations, this increase seems to be a result of spreading and a long term

wetting delay as depicted in Fig. 4.11. As the spherical drop on the probe starts to wet the substrate, the minimum radius increases, as from the left to right in Fig. 4.11. As the fluid wets the surface more, the minimum radius decreases, as in the right hand part of Fig. 4.11. The surprising result in Fig 4.10 is the time it takes to reach the maximum force. As water diffuses through the substrate in the radial direction, the contact angle must decrease. This allows for the fluid bridge to change shape.

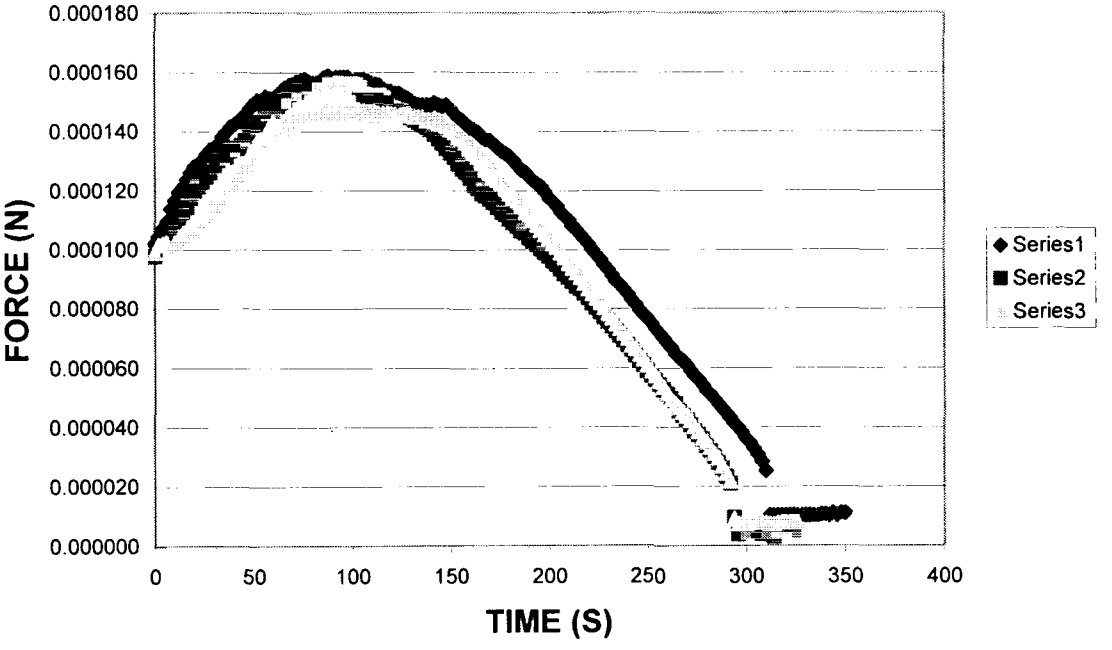

Figure 4.11: Force-time result for media C. Results in March.

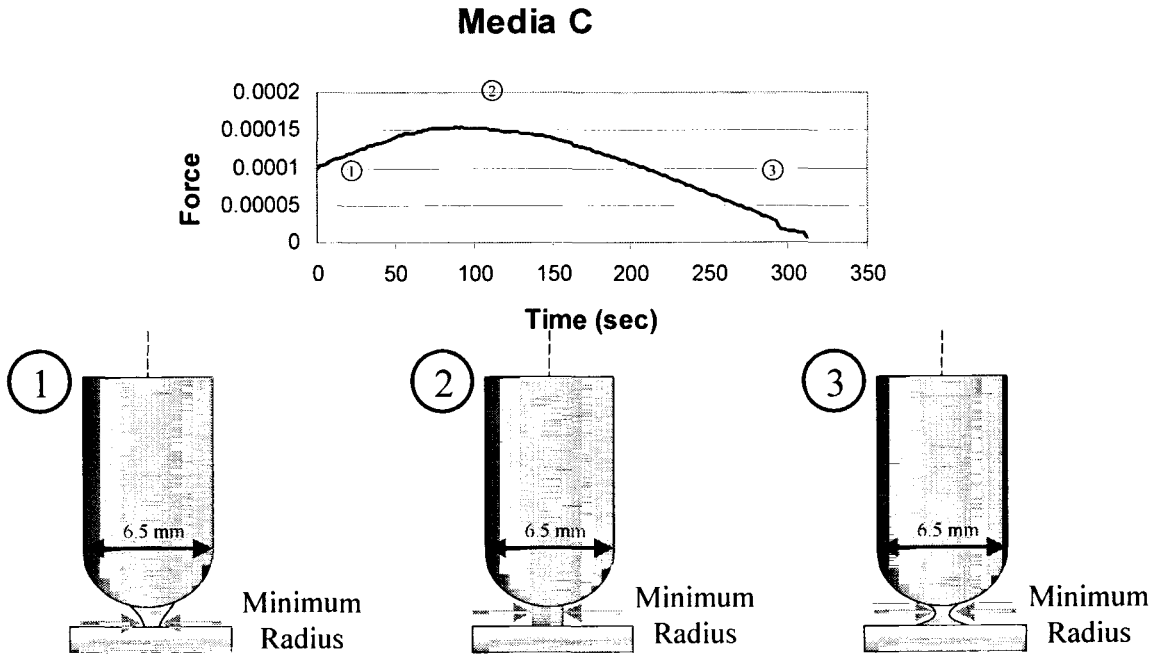

Figure 4.12: Shape of bridge as fluid wets and spreads on substrates.

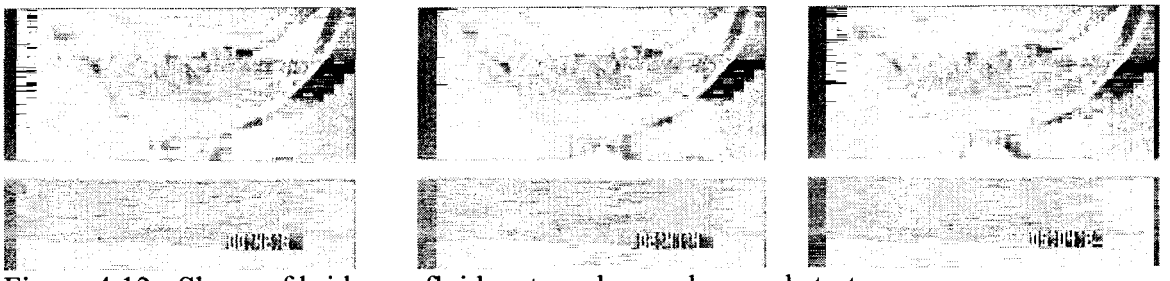

Figure 4.13: Shape of bridge as fluid wets and spreads on substrate.

Figure 4.11 shows the results of Media C taken in March, when the humidity in the room is assured to be low. Figure 4.4 is taken in July. Under humid conditions the difference is dramatic and point out the sensitivity of the test.

4.4 Force vs. contact angle

The minimum radius of the fluid determines the magnitude of the force between the probe and the substrate. When considering the geometry of the fluid bridge, we conclude that when the contact angle of the fluid with the substrate is at 90°, r_{min} is at a maximum. For contact angles greater or less than 90°, r_{min} will be lower and result in a lower force (see Fig 4.12). The contact angle between the fluid and the substrate is a direct result of the surface tension of the fluid and the surface energy of the substrate. The plot of force versus contact angle for the swellable substrates (Fig. 4.14) confirms the increase in force as the contact angle increases although for there is a decrease in the force before 90° is reached.

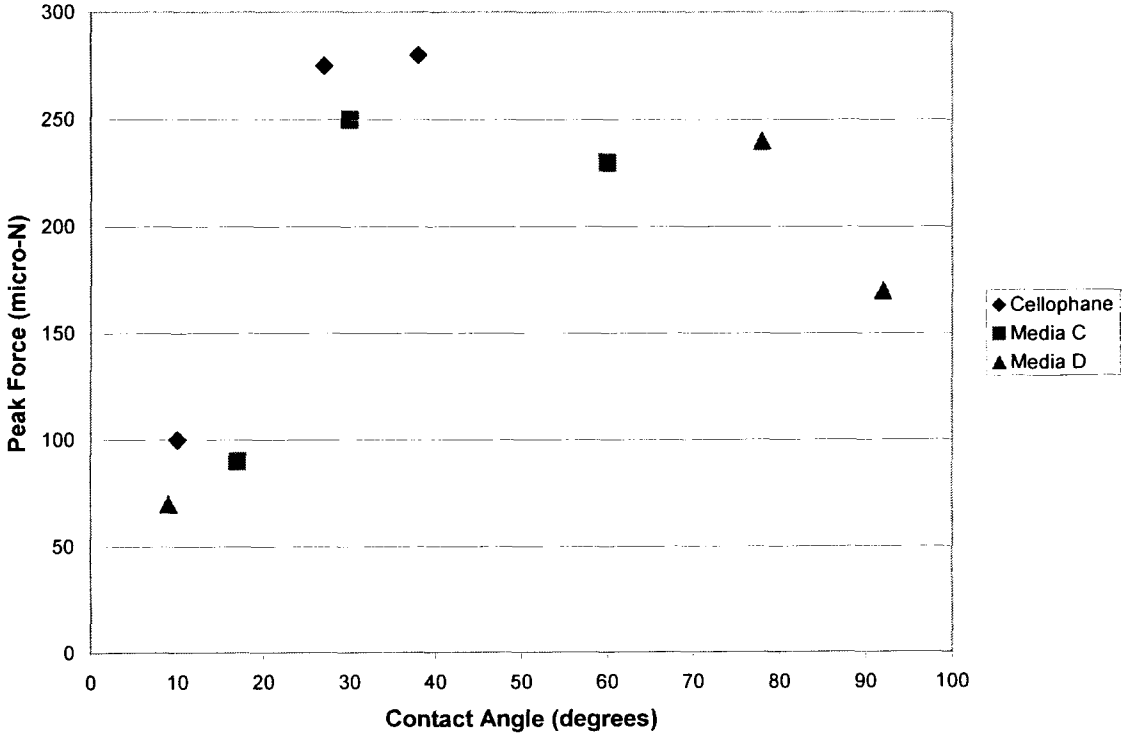

Figure 4.14: Plot of Peak force vs. contact angle for water, silicon oil, and ethylene glycol on the three swellable substrates at a gap of 0.35 mm.

4.5 Summary

Several interesting observations were made for the micro-probe test on substrates that take up fluid by diffusion. When water is applied to some substrates, the force will increase to a maximum and then decrease. For the force to increase there must be an increase in the maximum radius of the fluid column. The increase in the minimum radius and the subsequent increase in force is found to be caused by a contact angle and surface wetting phenomenon. As the water diffuses through the substrate in the radial direction, the contact angle decreases. When the contact angle drops below 90^{o}, the force will begin to decrease.

This test method is found to be very sensitive to humidity conditions. Figures 4.4 and 4.11 show the exact same test conditions but drastically different results.

Chapter 5: Real Substrates

5.1 Introduction

The ultimate goal for this project is to be able to apply this test method to real industrial situations. One application would be to characterize paper coating absorption uniformity to detect back-trap mottle problems shortly after manufacture. Theses "real" substrates are much more complex than the model substrates because they contain a range of materials. Paper is a composite material with wet end additives and possible sizing chemicals. Paper is coated with clay, calcium carbonate, plastic pigments, various binders, and additives. This test is not limited to paper substrates. Any surface can be analyzed with this test method.

5.2 Mottle samples

In order to apply this test to an actual situation, a sample set of coated papers that have various degrees of back-trap mottle problems are chosen. The samples are chosen because their surface characteristics are well known, and have varying back-trap-mottle problems as described by Xiang and coworkers (1998). The sample set of eight coated papers with varying degrees of mottle, determined by a panel of experts in print quality is investigated. The rating scale goes from 1 to 5 where 1 is the best and 5 is the worst. Magnitude and standard deviations of the force/time slopes, peak force, and force difference were recorded for 15 sample points within each of the eight samples. One micro-liter of Silicon oil is applied to the glass probe and the probe was positioned at

0.17 mm from the surface. The probe was applied the surface for five minutes. The peak force that results from the initial contact is recorded. Five minutes later the final force is recorded. Of interest is the variation within the surface of the sample. Therefore, the standard deviations of both the peak force and the slope of the force time curve are calculated for 15 different positions located approximately 10 mm apart.

Figures 5.1 and 5.2 show the correlation of the standard deviation in peak force and slope as a function of mottle rating. There may be, a small correlation in the standard deviation of the peak force with the mottle rating of the paper samples, but the correlation coefficient value is quite low. The trend is going in the direction that would be expected, in that a large variation would indicate back-trap mottle problem. The results using the standard deviation of the slope show no correlation and had the wrong trend.

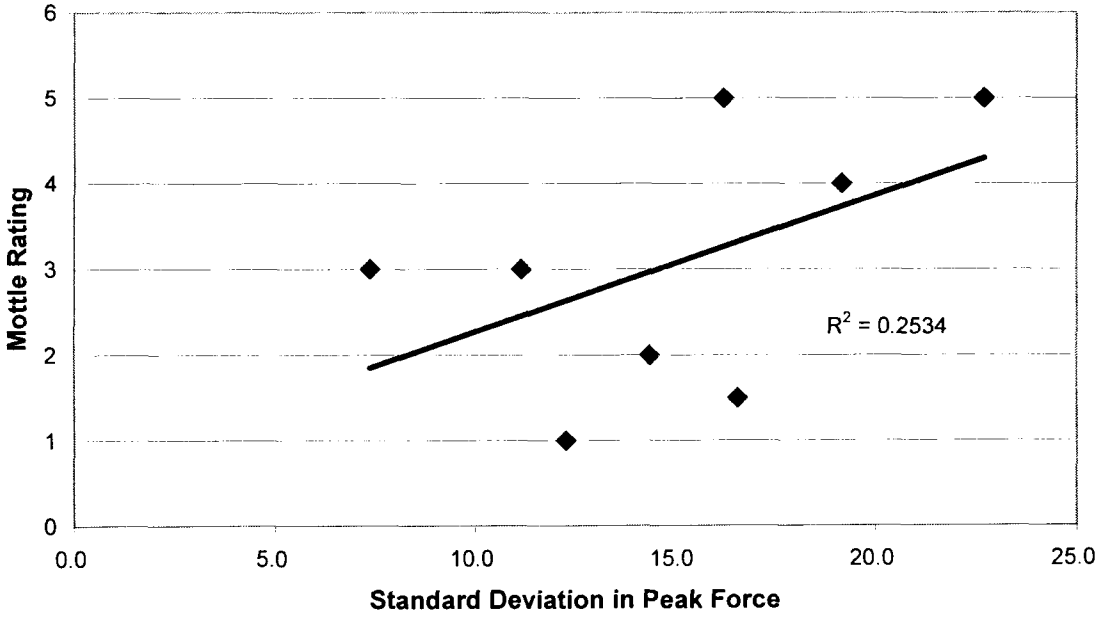

Figure 5.1: Correlation of the standard deviation in the peak force vs mottle rating.

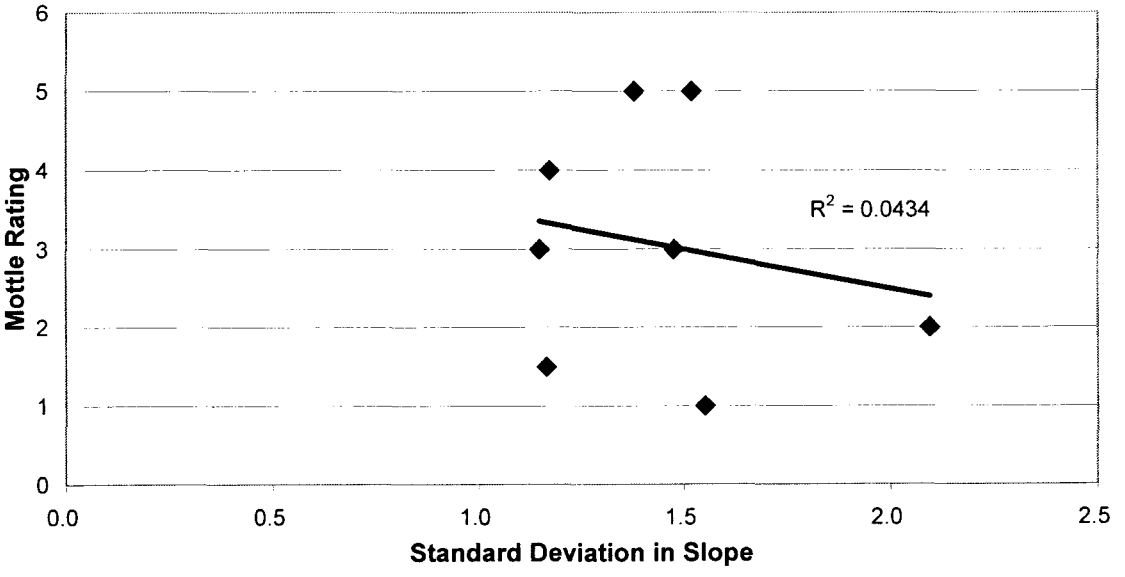

Figure 5.2: Correlation of the standard deviation in the slope of the force/time curve versus the mottle rating.

There were no conclusive trends that would help us distinguish between samples even though Xiang *et. al*, (1998) using the Micro-Tack tester, did pick up a nice correlation between ink setting rate variation and mottle using a 1.1 mm probe . The reason is expected to be caused by the radial penetration behavior of the test. The footprint on a 1.0 μL drop is about 1.5 mm across where as the size of the mottle variations is on the order of 0.7 mm. A smaller probe and a smaller volume fluid bridge are proposed to overcome this issue and give better results.

Ethylene glycol is used to replace silicon oil because it's higher surface tension makes it easier to apply to the probe in a consistent manner use. A 0.2 μL drop is applied to the

same glass probe. The distance is increased to 0.4 mm in order to minimize the diameter of the fluid footprint. Figures 5.3 and 5.4 show the correlation of the standard deviation in peak force and slope with mottle rating. There is no correlation in the standard deviation of the peak force with the mottle rating. The two papers with the lowest mottle ratings have the two lowest standard deviations. The sample with the highest mottle ratings had the highest standard deviation in the slope of the force-time response. However, the correlation coefficient is small between the standard deviation in the slope and the mottle rating. The correlation is not good enough to be used industrially.

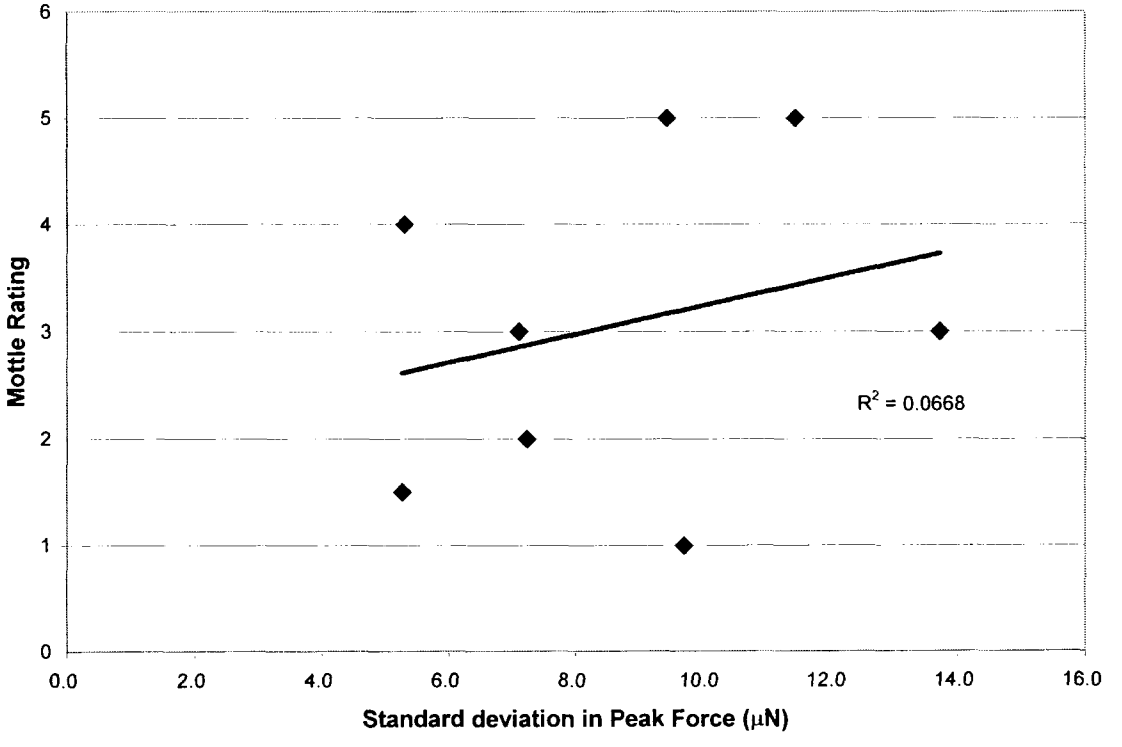

Figure 5.3: Correlation of the standard deviation in the peak force versus mottle rating using ethylene glycol as the test fluid.

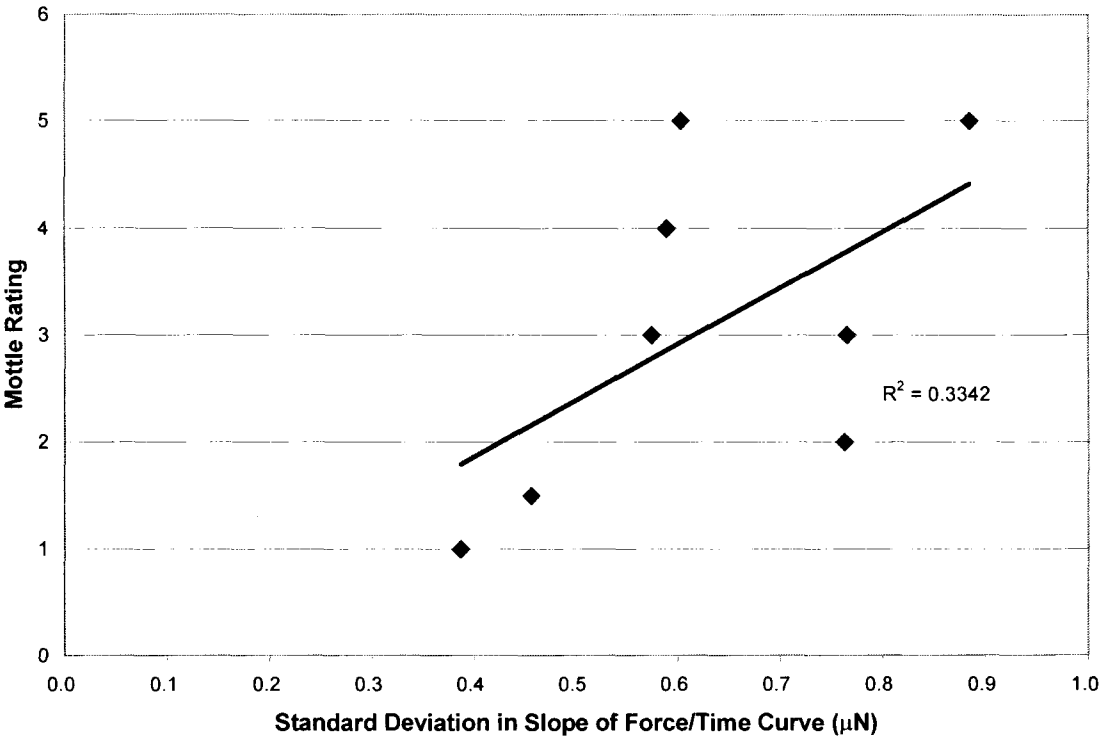

Figure 5.4: Correlation of the standard deviation in the slope of the force/time curve versus the mottle rating using ethylene glycol as the test fluid.

The mottle score of a sample is given by an expert group of people who based on the visual properties of the printed sample. Therefore, the mottle rating is not expected to have a good correlation with absorptive characteristics. The footprint of this new method is still about 1.0 mm. Radial spreading dominates the response. Also, the fluid must absorb into the underlying base paper and the test may be looking at the absorption into the base paper.

5.3 Other paper grades

The results of water on copy paper are shown in Fig. 5.5. This paper is sized to some degree. When water is used as the model fluid, the force gradually increases due to the wetting delay. As time goes on, the surface energy of the substrate lower when contacted by the fluid. Because of this sample being a real substrate, there is much more variation from one point to the next.

The force/time response is similar to that of Media C seen in Fig. 4.11. Unlike the swellable media, when this sample was tested with silicon oil, it absorbed rapidly due to a high porosity. This result is thought to be a result of the low surface tension of silicon oil. The results with silicon oil are not shown, but the oil shows a rapid uptake and only a single point with a peak force. The liquid is pulled into the paper structure rapidly, even more rapidly than water.

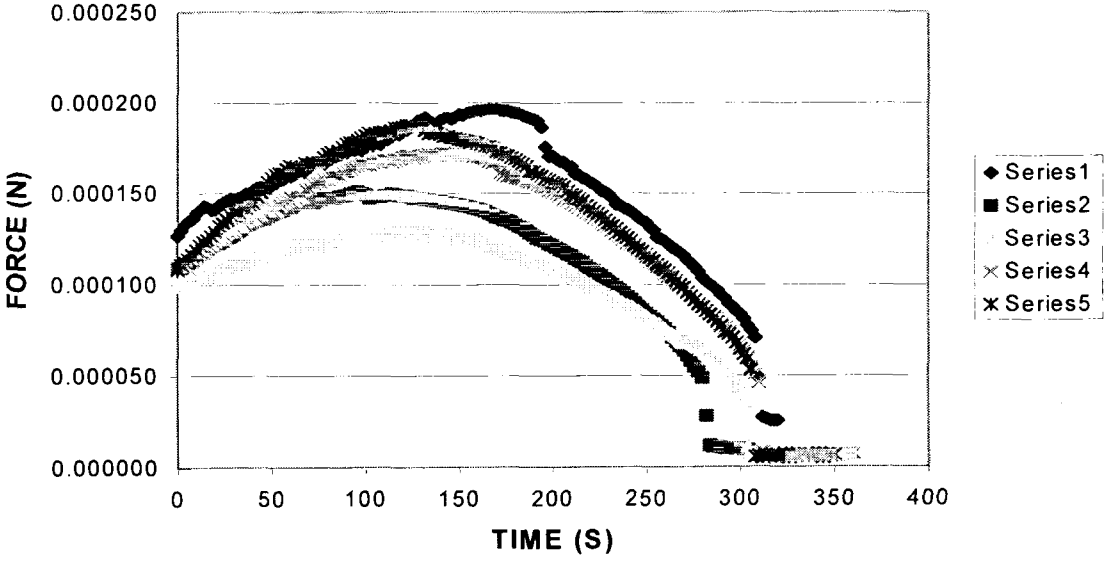

Figure 5.5: Results of water on copy paper.

This method was also used to a set of eight lightweight coated samples. The papers have a range of printing properties. Ethylene glycol is used under standard conditions as described in chapter 3. Each sample is tested at 5 locations. The average initial force, the average slope of the force-time curve, and standard deviations of both peak force and slope are calculated. The results of these tests are recorded in table 5.1.

	Avg Force (μN)	Stdev Force		Avg Slope	Stdev Slope	
A	299.2	11.3	4%	0.846	0.023	3%
B	304.4	24.8	8%	0.710	0.090	13%
C	306.6	17.6	6%	0.870	0.127	15%
D	299.5	23.1	8%	0.961	0.043	4%
E	315.4	15.8	5%	0.699	0.088	13%
F	300.7	14.0	5%	0.848	0.027	3%
G	297.7	8.2	3%	0.949	0.109	11%
H	303.7	15.9	5%	0.834	0.052	6%

Table 5.1: Initial force and slope calculations.

The initial force is determined by the height of the probe from the surface and the surface energy of the sample. The average peak force and the standard deviation of the peak force from one sample to the next is almost constant. Therefore, we can conclude that there is little difference in the surface energy from point to point within a sample. The slope of the force-time curve is result of the absorption of the test fluid into the substrate. Variations in the slopes of a given sample indicate non-uniformities in the absorption rate within the sample. From this data it is clear that there are differences the uniformity of the sheets. The test shows that samples B, C, F, and G had a higher degree of variation in absorption than the other samples.

Several uncoated papers were also tested but the results are not reported. Due to the absorbent nature of cellulose and cotton fibers, the test fluids reported here are taken up too rapidly to obtain meaningful data. For uncoated papers, ethylene glycol was absorbed too fast that no conclusions could be made with regard to the variation in porosity from one point to the next. For absorbent material, the event of absorption can be slowed down by the use of a more viscous test fluid, such as high viscosity silicon oils, corn syrup or glycerin.

5.4 Summary

The test method does have some promise to characterize the variability of absorption from point to point within a sample, but the length scale of the test may be too large to obtain a good correlation with back-trap mottle problems. The method does pick up differences between different samples, but uncoated samples absorb too rapidly using the fluids we tried.

Chapter 6: Conclusions and Future Work

A new method to evaluate local surface energy and porosity is developed. Analysis of the force-time data through a mathematical model representing the substrate gives understanding to the chemical and physical characteristics of the substrate. This test method has the capability of determining a local porosity and porosity variation within the plane of the surface.

On non-porous samples, the force is found to be a function of the surface tension of the fluid and the minimum bridge radius. The bridge radius is a function of how the fluid spreads on the surface and is a function of the substrate contact angle.

Porous substrates give an early peak force followed by a decrease. The peak force is related to the surface energy and thus contact angles, at short times. Decrease is related to the rate of absorption. A model is developed based on radial capillary flow to describe experimental results. While not perfect, the model does a good job at predicting experimental results. Swellable substrates show a range of results. For non-interacting fluids, a constant force is obtained. In some cases, the force slowly goes through a maximum; this behavior is related to the slow radial absorption that changes the contact angle of the substrate. For actual substrates, the test does pick up variations from point to point, but a good correlation with back-trap mottle rating was not obtained.

Further testing needs to be conducted with real substrates that have know printing defects in order to gain confidence that this method can detect the small scale variation in porosity of a given sample and then identify the defect. Using a smaller probe and a smaller amount of fluid should reduce the radial nature of the test and increase the normal component of absorption. The smaller probe may need to be attached to an Atomic Force Microscope device to detect the low forces.

Bibliography

Adamson A. W., "Physical Chemistry of Surfaces", John Wiley & Sons, Inc., chap 1, 5th Edition, 1990

Arai T., Yamasaki T., Suzuki K., Ogura T., Sakai Y., "Relationship between Coating Structure and Print Mottle", Proceedings of 1988 TAPPI Coating Conference, pp. 187-192

Aschan P., "Solving Problems of Print Mottle on Coated Board", Proceedings of 1986 TAPPI Coating Conference, pp. 73-75

Aspler J.S., Lepoutre P., "The Transfer and Setting of Ink on Coated Paper", Progress in Organic Coating, 1991, vol.19 pp. 333-357

Bird R.B., Stewart W.E., Lightfoot E.N., "Transport Phenomena", John Wiley & Sons, Inc., chap 6, 1960

Betchel S.E., Cooper J.A., Forest M.G., Peterson N.A., Reichard D.L., Saleh A., Venkataramanan V., "A New Model to Determine Dynamic Surface Tension and Elongational Viscosity Using Oscillating Jet Measurements", Journal of Fluid Mechanics, Vol 293, June 1995, p. 694-704

Box G., Hunter W., Hunter J., "Statistics for Experiments: An Introduction to Design, Data Analysis, and Model Building", Edition John Wiley & Sons, chap 17, 1978

Bristow J. A., "Liquid absorption into paper during short time intervals", Svensk Papperstidn, 1967, 70(19):623-629

Cassie A. B. D., Disc. Faraday Soc., Vol 3, 1948, p11

Elftson J. E., Strom G., "Penetration of aqueous solutions into models for coating layers", Coating Fundamentals Symposium, 1995, p17-25

Engstrom G., Norrdahl P., Strom G., "Studies of the Drying and Its Effect on Binder Migration and Offset Mottling", Proceedings of 1987 TAPPI Coating Conference, pp.35-43

Engstrom G., "Formation and Consolidation of a Coating Layer and the Effect on Offset-Print Mottle", Tappi J., vol.77, no.4, pp. 160-172

Fainerman V. B., Miller R., Joos P., "The measurement of dynamic surface tension by the maximum bubble pressure method", Colloid and Polymer Science, Vol. 272, No 6, 1994, p. 731-739

Gane P.A.C., Seyler E.N., "Tack Development: An Analysis of Ink/Paper Interaction in Offset Printing", Proceedings of 1994 TAPPI Coating Conference, pp. 243-260

Hiemenz P., Rajagopalan R., "Principles of Colloid and Surface Chemistry", Marcel Dekker, Inc., Third edition, 1997

Isoard J.C., "Ink Transfer and Retransfer – Mottling and Offset Picking of Coated Papers", Proceedings of 1983 TAPPI Coating Conference, pp.143-153

Israelachvili J.N., "Intermolecular & Surface Forces", Second Edition, 1992

Kumana A., Higuchi A., Watanabe T., Matsul H., "Reducing Mottle Through Coating Structure Design", Proceedings of 1993 TAPPI Coating Conference, pp. 1-8

LePoutre P., Rezanowich A., "Optical properties and structure of clay-latex coatings", TAPPI Journal Vol. 60, No.11, November 1977, p. 86-91

Louman H.K., "Mottling and Wettability", Proceedings of 1991 TAPPI Coating Conference, pp. 505-519

Lyne M.B., "The Mechanism of Backtrap Mottle", Proceedings of 1986 International Printing and Graphic Arts Conference, pp. 87-93

Mark R. E., "Handbook of Physical and Mechanical Testing of Paper and Paperboard", Marcel Dekker Inc., Vol. 2, chap 17, 1984

Marmur A., "Wetting on Real Surfaces", IS&T's 15th Int. Conf. Digital Print. Tech., 1999, p. 22-25

Mason G., Clark W.G., "Liquid bridges between spheres", Chem. Engng. Sci., Vol. 20, 1965, p. 859-866

Middleman S., "Modeling Axisymmetric Flows", Edition Academic Press, chap 4 & 7, 1995

Miwata H., Hattori Y., Ishikawa T., Yamazaki K., "Clarification of Print Mottle", Proceedings of 1995 TAPPI Coating Conference, pp. 231-246

Nelson R.E., "Sources of Backtrap Mottle", Proceedings of 1986 International Printing and Graphic Arts Conference, pp. 23-29

Nishioka T., Matsumoto, Uchida, A., Fujita K., "Analysis and Solution of Mottling Problems with Offset Printing", Proceedings of 1986 TAPPI Coating Conference, pp. 55-63

Oliver J.F., "Initial stages of ink jet drop impaction, spreading, and wetting on paper", TAPPI Journal Vol. 67, Oct. 1984, p. 90-94

Orr F.M., Scriven L.E., Rivas A.P., "Pendular rings between solids: meniscus properties and capillary force", Journal of Fluid Mechanics, Vol 67, 1975, p.723-742

Pasandideh-Fard M., Qiao Y.M., Chandra S. And Mostaghimi J. "Capillary effects during droplet impact on a solid surface", Phys. Fluids Vol 8, No.3, March 1996, p.650-659

Pitois O., Moucheront P., Chateau X., "Liquid Bridge between Two moving Spheres: An Experimental Study of Viscosity Effects", Journal of Colloid and Interface Science, Vol. 231, 2000, p.26-31

Plowman Sandreuter N., "Predicting Print Mottle: A Method of Differentiating Between Three Distinctively Different Types of Mottle: Back-trap Mottle, Water Sensitivity Mottle, and Wet Ink Trapping Mottle", Proceedings of 1994 TAPPI Coating Conference, pp. 211-227

Rayleigh Lord, "On the instability of jets", Proc. London Math. Soc., Vol 10, 1879, p.4

TAPPI Test Methods, "Air resistance of paper", T 460 om-88, Vol 1, 1991

Washburn W. E., "Note on a method of determining the distribution of pore sizes in a porous material" Proc. Nat. Acad. Sci., 1921, 7:115-116

Wenzel R. N., Ind & Eng. Chem., Vol. 28, 1936, p988

Whalen-Shaw M., Eby T., "A study of back-trap mottle in coated papers using electron probe microanalysis", Tappi J., vol.72, No.12, pp.188-194

Xiang Y., Bousfield D.W., Hassler J., Coleman P., Osgood A., "Measurement of Local Variation of Ink Tack Dynamics", Journal of Pulp and Paper Science Vol. 25, No. 9, September 1999, p.326-330

Xiang Y., Bousfield D.W., "The Cause of Backtrap Mottle: Chemical or Physical?", Proceedings from 2000 TAPPI Coating Conference, p.45-58

Xiang Y., Bousfield D.W., "Influence of Coating Structure on Ink Tack Dynamics", Journal of Pulp and Paper Science Vol. 26, No. 6, June 2000, p.221-227

Appendix A: Propagation of Error in Non-porous Force Calculation

Whenever a physical quantity is measured, there is a degree of uncertainty associated with the measurement. When several measured quantities are used in a mathematical relationship, there is a propagation of error that takes place. In this calculation, parameters of the fluid and fluid bridge are measured. The quantities are known to certain accuracy.

There is a certain amount of error and an accumulation of error with every measured value used in the determination of the force. In order to determine the contribution of each measured quantity and the total overall error in the theoretical calculation of the force, a least squares method is used.

Sample calculation of force for non-porous substrates

Diameter of fluid column $Dia := 0.0065 \quad m$

Surface tension of fluid $\sigma := 0.0728 \quad \frac{J}{m^2}$

Conversion factor $cf := \frac{0.97}{5.3}$

Force calculation $Force := \pi \cdot Dia \cdot cf \cdot \sigma$

$$Force = 2.721 \times 10^{-4} \quad N$$

Error Multiplying Factors

$$MFDia := \frac{d}{dDia}\pi \cdot Dia \cdot cf \cdot \sigma \qquad MFDia = 0.042$$

$$MF\sigma := \frac{d}{d\sigma}\pi \cdot Dia \cdot cf \cdot \sigma \qquad MF\sigma = 3.737 \times 10^{-3}$$

$$MFcf := \frac{d}{dcf}\pi \cdot Dia \cdot cf \cdot \sigma \qquad MFcf = 1.487 \times 10^{-3}$$

Estimated Measurement Errors

$EEDia := 0.0002$

$EE\sigma := 0.001$

$EEcf := 0.01$

Errors

$EDia := MFDia \cdot EEDia \qquad EDia = 8.372 \times 10^{-6}$

$E\sigma := MF\sigma \cdot EE\sigma \qquad E\sigma = 3.737 \times 10^{-6}$

$Ecf := MFcf \cdot EEcf \qquad Ecf = 1.487 \times 10^{-5}$

Total Error

$$E_{total} := \sqrt{(EDia)^2 + (E\sigma)^2 + (Ecf)^2}$$

$$E_{total} = 1.747 \times 10^{-5} \quad N$$

The estimated measurement errors are determined according to the accuracy that they can be measured. For example, Dia, which is measured manually, and has an accuracy of +/- 0.02 mm. The product of the measurement error and the multiplying factor determines the estimated error in a particular parameter.

Appendix B: Mathematical Formulation of the Theoretical Model

When a given substrate is raised to the probe, the fluid on the tip of the probe contacts the substrate and creates a force of attraction between the probe and the substrate. The data acquired is force versus time. First, let us look at the physical situation as depicted in Figure B.1.

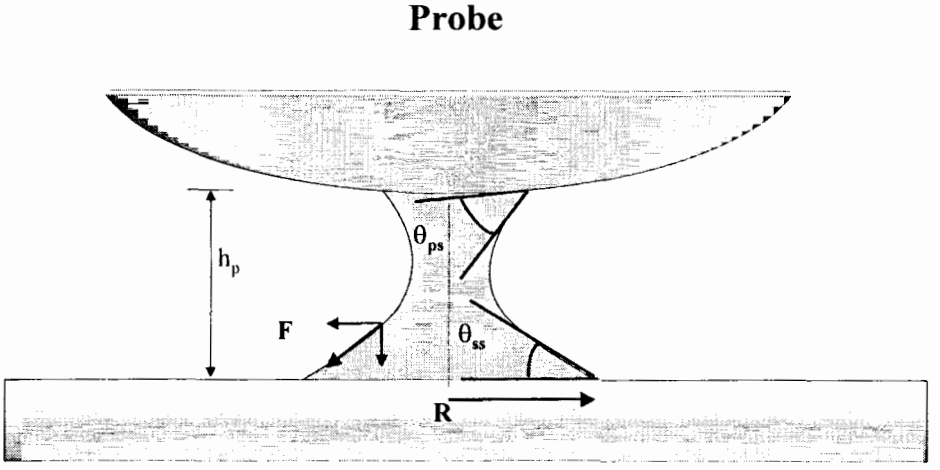

Figure B.1: Fluid bridging between the glass probe and the porous substrate

We know that for a static system with a non-porous substrate, equation 2.1 holds true. Now the substrate is no longer inert but the dynamic interaction between the fluid and substrate must now be a taken into account.

We start with a force balance on the surface of the fluid bridge. We know that the force on the surface of the fluid column must be the same anywhere on the surface. The vertical component of the force is dependent on the curvature of the fluid bridge. The relationship between the force at any given point on the curve and the radius of the fluid bridge is:

$$F = 2 \cdot \pi \cdot R \cdot \sigma \cdot \cos\theta \tag{B.1}$$

or

$$R = \frac{F}{2 \cdot \pi \cdot \sigma \cdot \cos\theta} \tag{B.2}$$

Where F is the vertical force component, R is the radius of the fluid column, σ is the surface tension of the fluid and θ is the angle deviation from vertical. The shape of the fluid bridge is determined by the volume of fluid between the probe and the substrate in conjunction with the fluid-probe contact angle θ_{ps}, and the fluid-substrate contact angle θ_{ss}. We see that by integrating the radial function through the height of the probe h_{ps}, we can calculate the volume of the fluid bridge V, by equation:

$$V = \int_0^{h_{ps}} (\pi \cdot R^2) dh \tag{B.3}$$

By inserting equation 3.2 into equation 3.3 the result is:

$$V = \pi \int_{\theta_{ss}-90}^{90-\theta_{ps}} \left(\frac{F}{2 \cdot \pi \cdot \sigma \cdot \cos\theta}\right)^2 \left(\frac{F}{2 \cdot \pi \cdot \sigma \cdot \cos\theta}\right) d\theta \tag{B.4}$$

After integrating we get volume as a function of the characteristic parameters. Using the integrated function for volume and taking the derivative of it with respect to time t, we see the resulting fluid uptake rate:

$$\frac{dV}{dt} = 3 \cdot c_0 \cdot F^2 \frac{dF}{dt} \tag{B.5}$$

Where c_0 is a complex function of surface tension and contact angles. In order to eliminate the need for visual contact angle measurement, we will estimate c_0 as $\frac{V}{F_{max}^{\ 3}}$.

Equation B.5 can be rewritten as:

$$\frac{dF}{dt} = \frac{-\frac{dV}{dt}}{3 \cdot c_0 \cdot F^2} \tag{B.6}$$

This is a key relationship to understanding how the force recorded experimentally changes with a given fluid uptake régime. Because we are dealing with model porous media, let us assume that the coating layer of our porous substrate is comprised of uniformly sized spherical particles. Let us assume that the footprint of the liquid column is fixed, perfectly circular, and there is only radial spreading (no Z-directional penetration through the substrate). This is a good assumption because most samples have very thin porous structures that are saturated upon contact as depicted in Figure B.2.

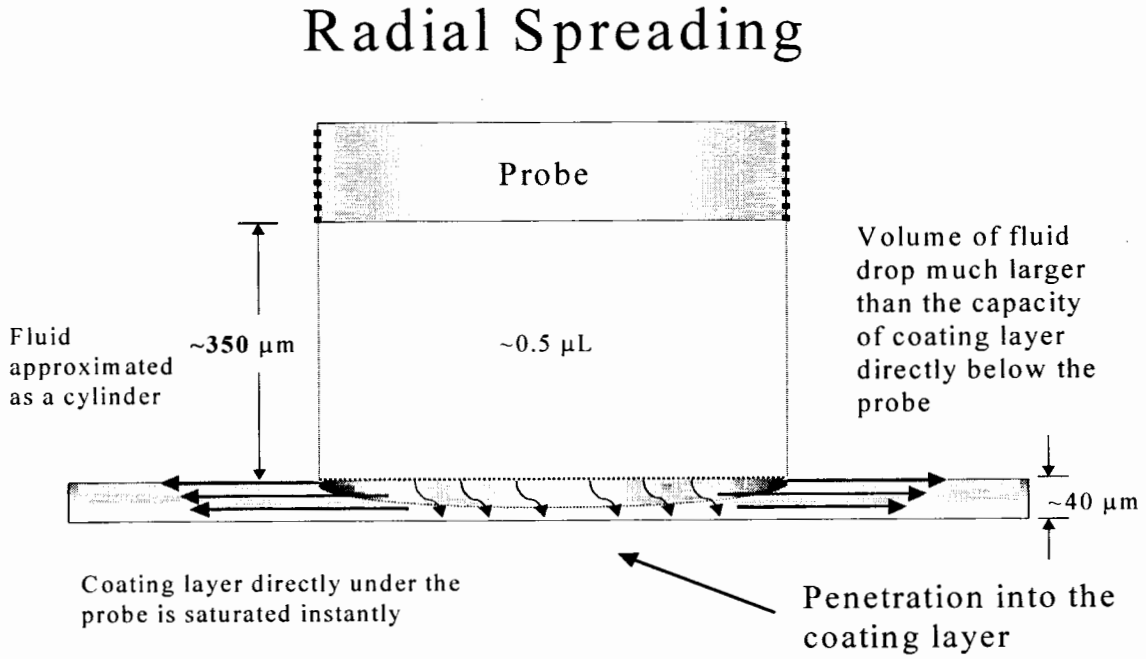

Figure B.2: Fluid instantaneously saturates coating then slowly spreads radially

Now if the flow in the radial direction of the porous material governs the fluid uptake then:

$$\frac{dV}{dt} = v_0 \cdot \pi \cdot D_S \cdot h_P \tag{B.7}$$

Where v_0 is:

$$v_0 = \frac{2 \cdot \Delta p}{(D_M - D_S)} \cdot \frac{d_p^{\,2}}{150 \cdot \eta} \cdot \frac{\varepsilon^3}{(1-\varepsilon)^2} \tag{B.8}$$

also

$$\Delta p = \frac{2 \cdot \sigma \cdot \cos\theta_{SS}}{r_p} \tag{B.9}$$

and

$$D_S = \frac{F}{\pi \cdot \sigma \cdot \sin\theta_{SS}} \tag{B.10}$$

Where d_p is the particle diameter inside the porous layer, D_M is the diameter of the liquid interface in the radial direction on the porous material, η is the viscosity of the fluid, ε is the void fraction of the porous layer, and r_p is the equivalent pore radius of the porous substrate. By defining Δp as in equation B.9, capillary forces drive the flow into the pores. Using this model we are assuming that the porous layer is behaving as a packed bed. When we combine equation B.6 and B.7 we get:

$$\frac{dF}{dt} = -\frac{\pi \cdot D_S \cdot h_p}{6 \cdot c_0 \cdot F^2} \cdot \frac{d_p \cdot \varepsilon^2}{(1-\varepsilon)} \cdot \left(\frac{2 \cdot \Delta p}{150 \cdot \eta}\right)^{\frac{1}{2}} \cdot d(\sqrt{t}) \tag{B.11}$$

After integrating, rearranging, and solving for the force, the resulting relationship is:

$$F_{\max}{}^3 - F_t{}^3 = \frac{\pi \cdot D_S \cdot h_p \cdot d_p \cdot \varepsilon^2}{c_0(1-\varepsilon)} \left(\frac{2 \cdot \Delta p}{150 \cdot \eta}\right)^{\frac{1}{2}} \cdot \sqrt{t - t_{\max}} \tag{B.12}$$

Where D_{SSo} is the diameter of wetting, F_{max} is the maximum force, and t_{max} is the time at the maximum force. If all of our assumptions are correct, when we plot $F_{\max}{}^3 - F_t{}^3$ vs $\sqrt{t - t_{\max}}$ the slope will be $\frac{\pi \cdot D_S \cdot h_p \cdot d_p \cdot \varepsilon^2}{c_0(1-\varepsilon)} \left(\frac{2 \cdot \Delta p}{150 \cdot \eta}\right)^{\frac{1}{2}}$.

Appendix C: Propagation of Error in Theoretical Model

Whenever a physical quantity is measured, there is a degree of uncertainty associated with the measurement. When several measured quantities are used in a mathematical relationship, there is a propagation of error that takes place. In this model, several properties of the fluid and the substrate are measured. The quantities are known to certain accuracy.

There is a certain amount of error and an accumulation of error with every measured value used in the determination of the theoretical slope. In order to determine the contribution of each measured quantity and the total overall error in the theoretical calculation of the slope, a least squares method is used.

To calculate the error contribution of one measured value, the partial derivative of the slope is taken with respect to that variable. That gives a factor which is multiplied by the estimated error in the measurement of that value. That product is squared to eliminate any negative signs and then the square root is taken to get the absolute value of the error contributed by that measured value.

Below is a sample calculation of error in measurements for the glass-silicon oil-722 scenario.

Error Multiplying Factors

$$MFDss_o := \frac{d}{dDss_o}\frac{\pi\cdot Dss_o\cdot h_p\cdot d_p\cdot\varepsilon^2\cdot F_{max}^3}{v\cdot(1-\varepsilon)}\cdot\left(\frac{4\cdot\sigma\cdot\cos(\theta ss)}{150\cdot\eta\cdot r_p}\right)^{\frac{1}{2}} \qquad MFDss_o = 2.386\times 10^{-9}$$

$$MFh_p := \frac{d}{dh_p}\frac{\pi\cdot Dss_o\cdot h_p\cdot d_p\cdot\varepsilon^2\cdot F_{max}^3}{v\cdot(1-\varepsilon)}\cdot\left(\frac{4\cdot\sigma\cdot\cos(\theta ss)}{150\cdot\eta\cdot r_p}\right)^{\frac{1}{2}} \qquad MFh_p = 1.527\times 10^{-9}$$

$$MFd_p := \frac{d}{dd_p}\frac{\pi\cdot Dss_o\cdot h_p\cdot d_p\cdot\varepsilon^2\cdot F_{max}^3}{v\cdot(1-\varepsilon)}\cdot\left(\frac{4\cdot\sigma\cdot\cos(\theta ss)}{150\cdot\eta\cdot r_p}\right)^{\frac{1}{2}} \qquad MFd_p = 3.394\times 10^{-6}$$

$$MF\varepsilon := \frac{d}{d\varepsilon}\frac{\pi\cdot Dss_o\cdot h_p\cdot d_p\cdot\varepsilon^2\cdot F_{max}^3}{v\cdot(1-\varepsilon)}\cdot\left(\frac{4\cdot\sigma\cdot\cos(\theta ss)}{150\cdot\eta\cdot r_p}\right)^{\frac{1}{2}} \qquad MF\varepsilon = 1.584\times 10^{-11}$$

$$MFv := \frac{d}{dv}\frac{\pi\cdot Dss_o\cdot h_p\cdot d_p\cdot\varepsilon^2\cdot F_{max}^3}{v\cdot(1-\varepsilon)}\cdot\left(\frac{4\cdot\sigma\cdot\cos(\theta ss)}{150\cdot\eta\cdot r_p}\right)^{\frac{1}{2}} \qquad MFv = -3.054\times 10^{-3}$$

$$MFF_{max} := \frac{d}{dF_{max}}\frac{\pi\cdot Dss_o\cdot h_p\cdot d_p\cdot\varepsilon^2\cdot F_{max}^3}{v\cdot(1-\varepsilon)}\cdot\left(\frac{4\cdot\sigma\cdot\cos(\theta ss)}{150\cdot\eta\cdot r_p}\right)^{\frac{1}{2}} \qquad MFF_{max} = 1.992\times 10^{-8}$$

$$MF\eta := \frac{d}{d\eta}\frac{\pi\cdot Dss_o\cdot h_p\cdot d_p\cdot\varepsilon^2\cdot F_{max}^3}{v\cdot(1-\varepsilon)}\cdot\left(\frac{4\cdot\sigma\cdot\cos(\theta ss)}{150\cdot\eta\cdot r_p}\right)^{\frac{1}{2}} \qquad MF\eta = -1.527\times 10^{-10}$$

$$MF\theta ss := \frac{d}{d\theta ss}\frac{\pi\cdot Dss_o\cdot h_p\cdot d_p\cdot\varepsilon^2\cdot F_{max}^3}{v\cdot(1-\varepsilon)}\cdot\left(\frac{4\cdot\sigma\cdot\cos(\theta ss)}{150\cdot\eta\cdot r_p}\right)^{\frac{1}{2}} \qquad MF\theta ss = -1.484\times 10^{-13}$$

$$MF\sigma := \frac{d}{d\sigma}\frac{\pi\cdot Dss_o\cdot h_p\cdot d_p\cdot\varepsilon^2\cdot F_{max}^3}{v\cdot(1-\varepsilon)}\cdot\left(\frac{4\cdot\sigma\cdot\cos(\theta ss)}{150\cdot\eta\cdot r_p}\right)^{\frac{1}{2}} \qquad MF\sigma = 2.133\times 10^{-11}$$

$$MFr_p := \frac{d}{dr_p}\frac{\pi\cdot Dss_o\cdot h_p\cdot d_p\cdot\varepsilon^2\cdot F_{max}^3}{v\cdot(1-\varepsilon)}\cdot\left(\frac{4\cdot\sigma\cdot\cos(\theta ss)}{150\cdot\eta\cdot r_p}\right)^{\frac{1}{2}} \qquad MFr_p = -5.09\times 10^{-6}$$

Estimated Measurement Errors

Errors

$EEDss_0 := 0.0001$	$EDss_0 := MFDss_0 \cdot EEDss_0$	$EDss_0 = 2.386 \times 10^{-13}$
$EEh_p := 0.0005$	$Eh_p := MFh_p \cdot EEh_p$	$Eh_p = 7.636 \times 10^{-13}$
$EEd_p := 0.0000002$	$Ed_p := MFd_p \cdot EEd_p$	$Ed_p = 6.787 \times 10^{-13}$
$EE\varepsilon := 0.02$	$E\varepsilon := MF\varepsilon \cdot EE\varepsilon$	$E\varepsilon = 3.168 \times 10^{-13}$
$EEv := 0.00000000001$	$Ev := MFv \cdot EEv$	$Ev = -3.054 \times 10^{-14}$
$EEF_{max} := 0.000001$	$EF_{max} := MFF_{max} \cdot EEF_{max}$	$EF_{max} = 1.992 \times 10^{-14}$
$EE\eta := 0.0005$	$E\eta := MF\eta \cdot EE\eta$	$E\eta = -7.636 \times 10^{-14}$
$EE\theta ss := 1$	$E\theta ss := MF\theta ss \cdot EE\theta ss$	$E\theta ss = -1.484 \times 10^{-13}$
$EE\sigma := 0.001$	$E\sigma := MF\sigma \cdot EE\sigma$	$E\sigma = 2.133 \times 10^{-14}$
$EEr_p := 0.0000000066$	$Er_p := MFr_p \cdot EEr_p$	$Er_p = -3.36 \times 10^{-14}$

Total Error

$$E_{total} := \sqrt{(EDss_0)^2 + (Eh_p)^2 + (Ed_p)^2 + (E\varepsilon)^2 + (Ev)^2 + (EF_{max})^2 + (E\eta)^2 + (E\theta ss)^2 + (E\sigma)^2 + (Er_p)^2}$$

$$E_{total} = 1.11 \times 10^{-12}$$

The estimated measurement errors are determined according to the accuracy that they can be measured. For example, F_{max}, which is measured on the Sigma70, reads to an accuracy of +/- 1 micro Newton. The estimated errors in the particle diameter d_p, changes depending on the substrate. The wafers of plastic pigment formed on Teflon are comprised of polystyrene spheres. Due to manufacturing restraints, the larger size (0.45 μm) polystyrene spheres have a larger particle size distribution where the smaller (0.1 μm) polystyrene spheres have a very uniform particle size. Due to the uncertainty in

particle diameter, it is assumed that the error in the 0.45 μm, 0.23 μm, and the 0.1 μm spheres is 0.2, 0.05, and 0.01 μm respectively.

Biography of the Author

Joshua Mathews was born in Waterville, Maine on November 11, 1975. He was raised in Pittsfield, Maine and graduated from Maine Central Institute in 1994. He attended The University of Maine and graduated in 1998 with a Bachelor's degree in Chemical Engineering and a minor in Chemistry. He entered the graduate program at The University of Maine in the fall of 1998.

After receiving his degree, Joshua will be seeking employment to begin his career in the field of industrial surface science. Joshua is a candidate for the Master of Science degree in Chemical Engineering from The University of Maine in May, 2001.